Titre: Title:	Rotor Wake Modelling Using the Vortex-Lattice Method
Auteur: Author:	Carlo Ferlisi
Date:	2018
Type:	Mémoire ou thèse / Dissertation or Thesis
Référence: Citation:	Ferlisi, C. (2018). Rotor Wake Modelling Using the Vortex-Lattice Method [Master's thesis, École Polytechnique de Montréal]. PolyPublie. https://publications.polymtl.ca/3059/

UNIVERSITÉ DE MONTRÉAL

ROTOR WAKE MODELLING USING THE VORTEX-LATTICE METHOD

CARLO FERLISI
DÉPARTEMENT DE GÉNIE MÉCANIQUE
ÉCOLE POLYTECHNIQUE DE MONTRÉAL

MÉMOIRE PRÉSENTÉ EN VUE DE L'OBTENTION
DU DIPLÔME DE MAÎTRISE ÈS SCIENCES APPLIQUÉES
(GÉNIE AÉROSPATIAL)
AVRIL 2018

UNIVERSITÉ DE MONTRÉAL

ÉCOLE POLYTECHNIQUE DE MONTRÉAL

Ce mémoire intitulé :

ROTOR WAKE MODELLING USING THE VORTEX-LATTICE METHOD

présenté par : FERLISI Carlo
en vue de l'obtention du diplôme de : Maîtrise ès sciences appliquées
a été dûment accepté par le jury d'examen constitué de :

M. SAUSSIÉ David, Ph. D., président
M. LAURENDEAU Éric, Ph. D., membre et directeur de recherche
M. PROTHIN Sébastien, Doctorat, membre

ACKNOWLEDGEMENTS

I would like to thank my research supervisor, Professor Éric Laurendeau, for his support and guidance throughout the project. His vision and knowledge created this opportunity for me, for which I am grateful.

I would also like to thank CAE Inc. and the *Natural Sciences and Engineering Research Council of Canada* (NSERC) for their financial support, without which this project would not have been possible. To Mike Theophanides, Olivier Soucy and Pierre-Olivier Tardif, from CAE, and to Professor Siva Nadarajah, from McGill, thank you for your support throughout this process. Your experience and input were indispensable to this project.

I would also like to thank my colleagues Réda, Vincent, Matthieu, Atanas, Miguel, Julien, Frédéric, Simon, Pierre and Anthony. The group's unity and its willingness to help each other made this process an incredible experience. Thank you for all your help. I hope that I may one day return the favour.

Last, but definitely not least, I would like to thank my family. Dino, Giannina, Gino, Antoinette, Tony, Pina, Sabrina, Marie-Hélène, words cannot express how grateful I am for everything you have done for me. Just know that everything I am, everything I've accomplished or ever will accomplish, it is because of you. I love you all.

RÉSUMÉ

Le but de ce travail est de débuter le développement d'un modèle aérodynamique de basse-fidélité à moyenne-fidélité pour la simulation de vol d'hélicoptères. Le travail est limité à l'étude de rotors en vol stationnaire, en vol axial (montée) et en effet de sol. La méthode de réseau de vortex instationnaire (UVLM) a été choisie comme plateforme de développement. Deux modèles de sillage basés sur la loi de Biot-Savart sont étudiés : le sillage classique de panneaux, tel que présenté par Katz et Plotkin, et le sillage de particules de vorticité (vortons), tel que présenté par Winkelmans et Leonard. Pour fidèlement représenter le sillage d'un hélicoptère, quatre modèles à noyau visqueux ont été implémentés pour enlever les singularités de la méthode UVLM. Les modèles Lamb-Oseen, Scully et Vatistas sont utilisés pour le modèle de sillage de panneaux, alors que le modèle de lissage algébrique est utilisé pour le sillage à vortons. Le sillage est convecté librement dans l'air, permettant l'enroulement du sillage en bout de pale, ainsi que des effets instationnaires.

Les modèles à noyau visqueux sont comparés à l'aide du rotor de Caradonna-Tung. Le modèle de Lamb-Oseen est le plus rapide à converger en génération de poussée pour le sillage classique de panneaux. Toutefois, le sillage composé de particules de vorticité est le plus stable dans la génération de poussée. Il permet également la convergence en traînée (puissance requise du moteur), permettant le calcul de l'indicateur de qualité du rotor. La position du sillage développé par ces deux méthodes converge également.

Des simulations utilisant un sillage composé de vortons sont comparées aux résultats expérimentales du rotor de Caradonna en montée. L'indicateur de qualité obtenu par la simulation est surestimé en comparant aux mesures expérimentales. Ce résultat est attendu, car la UVLM utilise une approche non visqueuse. Le couplage de cette méthode à une base de données visqueuse est proposé.

Le modèle de sillage utilisant des vortons est ensuite comparé aux résultats expérimentales du rotor anticouple du Lynx en effet de sol. Une augmentation de la poussée générée par le rotor est obtenue en approchant le rotor du sol, en accord avec les résultats expérimentales. La convergence devient problématique lorsque le rotor s'approche du sol. Des effets instationnaires, tels que la génération d'anneaux de vorticité près du moyeu du rotor, sont capturés.

Ce travail est conclu en résumant le travail accompli et en énonçant les limitations du modèle. Des recommandations pour le développement du modèle sont ensuite proposées.

ABSTRACT

The purpose of this work is to begin the development of a low-fidelity to medium-fidelity aerodynamic model for rotorcraft for flight simulation. This work is limited to the study of rotors in hover, axial flight (climb) and hover in ground effect. The Unsteady Vortex-Lattice Method (UVLM) is selected as the development platform. Two wake models based on the Biot-Savart law are studied: the classic panel wake, as presented by Katz and Plotkin, and the vortex particle (or vorton) wake, as presented by Winkelmans and Leonard. In order to correctly model the wake for rotorcraft applications, four viscous core models are implemented to remove the singularities present in the UVLM. The Lamb-Oseen, Scully and Vatistas core models are used for the classic panel wake, while the algebraic core smoothing model is used for the vorton wake. The free-wake methodology is used to convect the wake with the flow field, allowing tip roll up and the capture of unsteady effects.

The viscous core models are compared using the Caradonna-Tung rotor. The Lamb-Oseen core model proves to converge the quickest in thrust for the panel wake methods. The vortex particle wake, however, is found to be the most stable in thrust. It also allows convergence in drag (torque), allowing the calculation of the Figure of Merit. The wake developed using the Lamb-Oseen and vortex particles showed convergence in the position of the tip vortex.

The vortex particle wake is used to compare simulation results to the Caradonna rotor in climb. The Figure of Merit calculated by the simulation is shown to overestimate the value measured in experiments. This is expected, as the UVLM is an inviscid approach. Further investigation into viscous coupling algorithms is proposed.

The vortex particle wake is also compared to the Lynx tail rotor in ground effect. Increase in the thrust generated by the rotor when approaching the ground is seen in the simulation data, agreeing with experimental data. Convergence becomes an issue as the rotor approaches the ground. Unsteady phenomena, such as the creation of vortex rings near the rotor hub, are captured.

The work is concluded by summarizing the described work and stating the current limitations of the model. Recommendations for future work are then proposed.

TABLE OF CONTENTS

LIST OF TABLES

LIST OF FIGURES

LIST OF ACRONYMS AND ABBREVIATIONS

CFD	Computational Fluid Dynamics
UVLM	Unsteady Vortex-Lattice Method
RANS	Reynolds Averaged Navier-Stokes
SLVE	Straight-Line Vortex Element
URANS	Unsteady Reynolds Averaged Navier-Stokes

CHAPTER 1 INTRODUCTION

The prediction of aerodynamic forces on aircraft in early design phases is a problem of great importance to the aerospace industry. The rapid development of technology has permitted the use of increasingly complex aerodynamic models with ever-increasing precision. This increased precision still comes at a cost in the form of increased computational time and memory requirements. In the detailed design phase, higher fidelity aerodynamic models are required to refine early design choices. However, not all applications require the level of detail granted by high fidelity models. For example, in the optimization phase of a project, there are a large number of cases to study. If high fidelity models are used, the optimization process can become costly. At the expense of some physical accuracy, medium or low fidelity aerodynamic models may be used to reduce the design space until reaching an optimal design. High fidelity models would then be employed to validate and fine-tune the results from the lower fidelity models.

Another example of the limited use of high fidelity simulations would be the prediction of aircraft performance for flight simulators. Flight simulators need to run in a real-time runtime environment. Thus, the cost of high fidelity computational fluid dynamics limits its use in a flight simulation environment. This leads to loosely coupled simulations, where computational results generated "offline" (prior to simulation) and incorporated in the form of lookup tables inside a real-time environment (Lambertenghi *et al.*, 2015). Because of this limitation, the number of situations that may be simulated using high fidelity CFD is finite.

However, aerodynamic interaction in certain flight phases (e.g. helicopter landing on a ship or on an oil rig) is too fluid for the use of lookup tables. The flight simulation industry therefore has a need for simplified aerodynamic models to simulate these situations in real-time (Theophanides and Spira, 2009). These models often require a certain amount of tuning to meet pilot expectations. To reduce the amount of tuning required in these models, the growing tendency is to use medium fidelity aerodynamic models, such as the Vortex-Lattice Method, running in (or near) real-time (Horn *et al.*, 2006).

1.1 Basic Concepts

1.1.1 The Vortex-Lattice Method

Potential Theory

This thesis studies the use of the Vortex-Lattice Method as a medium fidelity to low fidelity CFD tool to predict helicopter performance characteristics. The Vortex-Lattice Method is based upon the assumption of an inviscid, incompressible and irrotational flow. With these hypotheses, the flow velocity field $\vec{u} = f(x, y, z)$ can be shown to be a potential field $\vec{u} = \nabla\Phi$. The continuity equation for an incompressible flow is

$$\nabla \cdot \vec{u} = 0, \tag{1.1}$$

which can now be rewritten as

$$\nabla \cdot \nabla\Phi = \nabla^2\Phi = 0. \tag{1.2}$$

The relation $\nabla^2\Phi = 0$ is also known as Laplace's equation. The solution to Laplace's equation can be a linear combination of multiple solutions to Laplace's equation. As such, certain primitive and simple solutions to this relation may be combined to create a more complex flow field. The most common solutions in the field of aerodynamics to Laplace's equation are:

- freestream (uniform) velocities,
- point sources / source panels,
- point doublets / doublet panels,
- vortex filaments/panels.

These elements generate a potential field, associated to a velocity field, in their vicinity. The reader is invited to refer to Anderson Jr (2010), Cummings *et al.* (1998) and Katz and Plotkin (2001) for a detailed review of these solutions.

System of Equations

The Vortex-Lattice Method can be seen as an extension to Prandtl's Lifting Line Theory. A wing is represented as a finite number of panels modelled along the airfoil camberline, creating a lifting surface. Figure 1.1 shows an example of the discretization of a rotor. The figure also

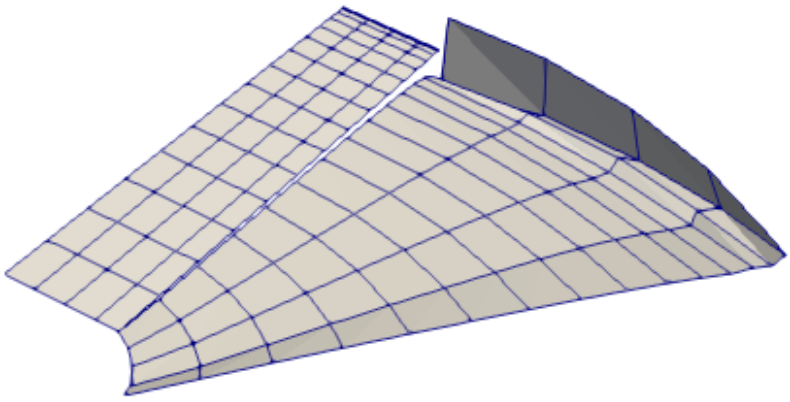

Figure 1.1 Discretization of a Single-Bladed Rotor into Panels with Free Wake

shows that the wake may be represented by vortex panels (also called vortex rings). Kelvin's theorem states that vorticity cannot be created in a closed system. In other words, vorticity cannot begin or end in a fluid; it must form a closed loop or extend toward infinity. To respect this condition, each panel is comprised of four vortex filaments of equal circulation Γ, forming a closed loop of vorticity. For simplicity, the circulation for each filament is referred to as the panel's vorticity. As previously stated, each vortex filament imparts a velocity on the surrounding flow. The circulation of a panel is directly related to the force it generates by applying the unsteady Bernouilli equation and Kutta-Joukowski theorem (Katz and Plotkin, 2001) :

$$\vec{F} = \rho \left(\|\vec{u}\| \, \Gamma + \frac{\partial \Gamma}{\partial t} \right) A \vec{n}, \tag{1.3}$$

where ρ is the fluid density, A is the area of the panel and $\vec{n}$ is the panel normal. The purpose of the VLM is to determine each panel's Γ to obtain the lift distribution along a wing. Whereas the vortex strength is unknown on the wing, the strength of the panels in the wake is known. In the steady (fully developed) case, the wake Γ is the same as the trailing edge panel from which each panel was shed. In the unsteady case, the strength is that of the trailing edge panel at the moment it was shed.

To evaluate the strength of each panel of the wing geometry, a system of equations is created based on the principle of non-penetrating flow through a panel. Mathematically, this is

represented as

$$\vec{u}_i \cdot \vec{n}_i = 0, \tag{1.4}$$

evaluated at the i^{th} panel's collocation point, where the i^{th} panel represents a physical geometric entity (e.g. a wing). The velocity at the panel's collocation point, $\vec{u}_i$, is subdivided as follows:

- the influence of other geometric panels onto panel i, or $\vec{u}_{j\to i}$,
- the influence of the wake panels onto panel i, or $\vec{u}_{k\to i}$,
- the freestream velocity U_∞,

where j is part of the same subset as i and k is part of the subset that represents wake panels of known strength. The velocity $\vec{u}_{\eta\to\xi}$ is calculated using the Biot-Savart law, which will be presented in section 3.1.1. For the purposes of this explanation, this equation can be modelled as a linear function of Γ, as shown here:

$$\vec{u}_{\eta\to\xi} = \vec{\zeta}_{\eta\to\xi}\Gamma_\eta. \tag{1.5}$$

The variable $\vec{\zeta}$ is a function of the relative position between the collocation point of panel ξ and the position and size of panel η. The system of equations can therefore be written as

$$\left(\sum_j \vec{\zeta}_{j\to i}\Gamma_j + \sum_k \vec{\zeta}_{k\to i}\Gamma_k + \vec{u}_\infty\right) \cdot \vec{n}_i = 0. \tag{1.6}$$

In vector form, this is rewritten as

$$\mathbf{A}\vec{\Gamma}_{Geometry} = \mathbf{B}\vec{\Gamma}_{Wake} + \vec{C}, \tag{1.7}$$

where

$$A_{i,j} = \frac{\vec{u}_{j\to i}}{\Gamma_j} \cdot \vec{n}_i, \tag{1.8}$$

$$B_{i,k} = -\frac{\vec{u}_{k\to i}}{\Gamma_k} \cdot \vec{n}_i, \tag{1.9}$$

$$C_i = -\vec{u}_\infty \cdot \vec{n}_i. \tag{1.10}$$

The system of equations is then solved for $\vec{\Gamma}_{Geometry}$ using a numerical solver.

1.2 Elements of the Problematic

1.2.1 Wake Proximity in Rotating Blades

One of the issues regarding the Vortex-Lattice Method for rotary-wing aircraft is the relative proximity of the wake to the lifting surfaces. While the wake in fixed-wing aircraft trails behind the wings, rotorcraft wake is pushed below the rotor. Depending on the flight regime, the wake may stagnate near the rotor blades. The VLM models this wake using singularity based elements. Thus, the proximity of the blades to the wake may lead to numerical divergence if they are too close together. This issue is also present within the wake, where rollup may bring wake panels together, also potentially leading to numerical divergence.

In hover, the rotor creates sufficient downwash to convect the inboard wake away from the rotor disk, partially alleviating this problem. Near the rotor tip, however, there is a large disparity in the lift generated by the rotating blade. This disparity causes a large vortex to shed from the blade tip that descends slower than the inboard wake. The tip vortex can pass sufficiently close to the blades to cause the solution to diverge.

In ground effect (when the rotor is placed within a few rotor radii of the ground), this problem is worsened, as the wake cannot propagate downwards freely. It is instead forced outboard of the rotor and compressed underneath it, thus bringing the wake closer together, again aggravating the singularity issue. Other wake instabilities also arise in ground effect, as is stated in the next section.

1.2.2 Wake Instabilities near the Ground

The movement of the rotor wake is restricted when close to the ground. The strongest elements of the wake tend to be ejected outboard when in proximity to the ground. However, there is a small portion that can remain beneath the rotor in a vorticity "bubble". In the Vortex-Lattice Method, the wake panels subjected to these diverging velocities lead to unrealistic wake geometries. The developed geometries quickly become chaotic and may lead to numerical divergence.

1.2.3 Computational Costs of the Unsteady Vortex-Lattice Method with Free-Wake

As previously stated, to successfully solve the system of equations created in the Vortex-Lattice Method, an N panel distribution also requires N equations to solve. The mutual interaction of the panels requires N^2 evaluations of the Biot-Savart equation, which is by far

the most time-consuming calculation of the VLM. In the Unsteady Vortex-Lattice Method, the algorithm begins with N_0 starting panels. At every timestep $i \in \mathbb{N}$, ΔN panels are shed into the wake. This requires $(N_0 + i\Delta N)^2 = N_0^2 + 2N_0 i\Delta N + i^2(\Delta N)^2$ evaluations of the Biot-Savart equation at timestep i. It is apparent that the problem complexity increases rapidly with each timestep calculated by the UVLM.

1.3 Objectives

The overarching objective of this research project is to develop a numerical model that can determine the performance parameters of a helicopter landing on a ship. Helicopter performance is closely related to its wake. The primary objective of this thesis is to accurately model helicopter wakes. This thesis attempts to accomplish this through the following sub-objectives:

- develop a model that can determine the performance of a helicopter in hover and climb;
- develop a model that can determine the performance of a helicopter in ground effect.

One of the project's restrictions was the use of the UVLM.

1.4 Plan of Thesis

This thesis is separated into three chapters:

- the literature review;
- the developments made within the UVLM code;
- the validation of the code.

To achieve the previously stated objectives within the provided framework, the following methodology was chosen:

- adapt in-house UVLM code to incorporate rotating lifting surfaces;
- study the effect of various viscous core models on helicopter performance and numerical stability;
- study the effect of various wake models on simulation accuracy.

Chapter 2 presents a literature review of various methods in the field of aerodynamics used to predict helicopter performance. The principles of Momentum Theory and Blade Element Theory are described. A review of models using the Biot-Savart equation is then presented. Finally, the accurate but time-consuming Navier-Stokes methods are presented.

Chapter 3 presents the developments and improvements made to the in-house UVLM code, provided by Professor Laurendeau's research group. The viscous core models used to prevent numerical singularities are detailed and verified. The use of the Vortex-Lattice Method in ground effect and near obstacles is then presented. Finally, the development of the vortex particle wake model is presented.

Chapter 4 validates the developed code against three classic test cases. The first is the Caradonna-Tung rotor in hover, as presented by Caradonna and Tung (1981). The presented rotor has two blades and is tested in hover. The resulting thrust coefficients and wake geometry are presented. The second is the Caradonna rotor in axial flight (Caradonna, 1999). The test uses a two-bladed rotor, placed in a wind tunnel to simulate climbing flight. The rotor's power requirements and wake geometry are presented. The third is the Lynx tail rotor, as presented by Light (1993). The four-bladed tail rotor is placed at varying distances from a flat plate and tests the effect of ground proximity on rotor performance. The thrust coefficients and rotor geometry are also presented, as well as the performance gain obtained in ground effect.

The thesis is then synthesized and recommendations are made for future work.

CHAPTER 2 LITERATURE REVIEW

This chapter presents a review of the current methods used in determining the aerodynamic forces on a helicopter rotor. The basic concepts of momentum theory and blade element theory are first explained. Models based on the Biot-Savart law, such as the Vortex-Lattice Method, are then shown, followed by grid-based models (e.g. Reynolds-Averaged Navier-Stokes).

2.1 Momentum Theory

Momentum theory is a low-fidelity model that calculates the maximum theoretical lift of a rotor. It also calculates the minimum theoretical power required to generate the predicted lift. It is based on Newton's second and third laws. Newton's second law states that a change in the momentum of a rigid body is caused by an external force:

$$\frac{d\left(m\vec{V}\right)}{dt} = \sum \vec{F}. \tag{2.1}$$

Newton's third law states that for every action, there is an equal and opposite reaction. In aerodynamics, an object in a flow field causes a change in momentum in the surrounding air. The object must therefore exert a force on the surrounding air, which subjects the object to an equivalent force in return. In the case of a helicopter, the main rotor's rotating blades push air downwards, through the rotor. The air must therefore push back on the rotor, generating lift and drag. Momentum theory requires the following assumptions:

- one-dimensional flow,
- inviscid flow,
- fully developed (steady) flow,
- uniform disk loading,
- low disk loading.

In momentum theory, a rotor is modelled as an infinitely thin disk that supports an increase in pressure across its surface, also known as an actuator disk. Figure 2.1 shows that the flow field for an actuator disk is one-dimensional. The flow is divided into four principal stations.

Station 0 is positioned far above the rotor, represented by the freestream velocity V and ambient pressure P_∞. Station 1 is positioned just above the rotor, where the pressure is P_U. Station 2 is positioned just below the rotor, with pressure P_L. The actuator disk induces an additional velocity v across the actuator disk. Station 4 is positioned far below the rotor, where the pressure is equalized to the ambient value and the velocity downstream is now $V + w$.

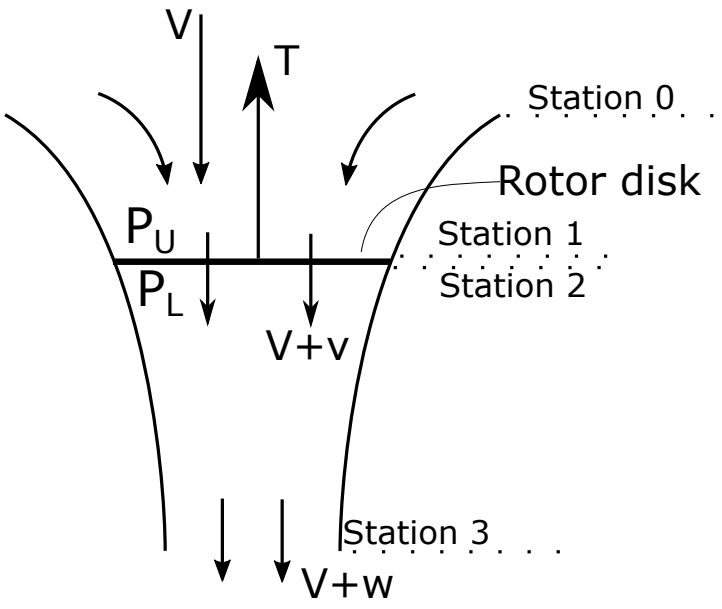

Figure 2.1 Momentum Theory Nomenclature

The thrust T developed by an actuator disk can be obtained by integrating the pressure over the rotor area $A = \pi R^2$, R being the rotor radius. In 1D flow, this is equivalent to

$$T_{ActuatorDisk} = A\left(P_L - P_U\right). \tag{2.2}$$

The thrust may also be obtained by calculating the change in momentum between stations 0 and 3.

$$T_{ActuatorDisk} = -\dot{m}(V - (V + w)), \tag{2.3}$$

$\dot{m}$ being the mass flow rate through the rotor. The mass flow rate is given by

$$\dot{m} = \rho v A, \tag{2.4}$$

where ρ is the air density.

Bernouilli's equation may be applied between stations 0 and 1

$$P_\infty + \frac{1}{2}\rho V^2 = P_U + \frac{1}{2}\rho\left(V+v\right)^2, \tag{2.5}$$

and between stations 2 and 3

$$P_L + \frac{1}{2}\rho\left(V+v\right)^2 = P_\infty + \frac{1}{2}\rho\left(V+w\right)^2. \tag{2.6}$$

Consider the case of hover, where $V = 0$ and $v = v_{Hover}$, $w = w_{Hover}$. Subtracting equation 2.5 from 2.6 in hover yields :

$$\frac{1}{2}\rho w_{Hover}^2 = P_L - P_U = \frac{T}{A}, \tag{2.7}$$

Substituting equation 2.7 into 2.3 in hover would therefore yield

$$\frac{T}{A} = \frac{1}{2}\rho w_{Hover}^2 = \rho v w, \tag{2.8}$$

or

$$w_{Hover} = 2v_{hover}. \tag{2.9}$$

Substituting equation 2.9 into equation 2.7, the following key result is obtained :

$$\frac{T}{A} = \frac{1}{2}\rho\left(2v_{Hover}\right)^2, \tag{2.10}$$

which simplifies to

$$v_{Hover} = \sqrt{\frac{T}{2\rho A}}. \tag{2.11}$$

The power P required to accelerate the flow through the actuator disk in hover is calculated using :

$$P_{Hover} = T v_{Hover} = T\sqrt{\frac{1}{2\rho}\frac{T}{A}}. \tag{2.12}$$

This formulation shows that the theoretical power is proportional to the square root of the disk loading. This result is similar to the aspect ratio for fixed-wing aircraft, where a higher aspect ratio reduces the theoretical power required to move the wing forward.

The dimensionless thrust and power coefficients are respectively defined as

$$C_T = \frac{T}{\rho A \left(\Omega R\right)^2}, \tag{2.13}$$

$$C_P = \frac{P}{\rho A \left(\Omega R\right)^3}, \tag{2.14}$$

where Ω is the rotational velocity of the rotor. The torque Q is related to the power required by the following equation:

$$P = Q\Omega, \tag{2.15}$$

The dimensionless torque coefficient is defined as

$$C_Q = \frac{Q}{\rho A R \left(\Omega R\right)^2}. \tag{2.16}$$

Note that C_P and C_Q are equivalent, a relationship that will be exploited later in the UVLM to calculate the power required for the rotor.

Equation 2.12 represents the power required for a rotor disk with assumed constant inflow velocity. As this is the ideal inflow distribution of a rotor, this power is the theoretical minimum (or ideal) power required to maintain hover. Equation 2.12 may be rewritten in its dimensionless form:

$$C_{P_{Ideal}} = \frac{C_T^{\frac{3}{2}}}{\sqrt{2}}. \tag{2.17}$$

The Figure of Merit FM is a measure of rotor efficiency. It relates the minimum power required to turn the rotor to the actual power required through the following equation:

$$FM = \frac{C_{P_{Ideal}}}{C_{P_{Real}}}. \tag{2.18}$$

The Bernouilli equation remains valid within a streamtube. The mass flow rate within this streamtube must therefore remain constant. The theoretical maximum contraction of the flow past the rotor disk is shown to be

$$A_{Station3} = \frac{1}{2} A_{Disk} \tag{2.19}$$

or

$$\left(\frac{r}{R}\right)_{Station3} = \sqrt{\frac{1}{2}} \approx 0.707, \tag{2.20}$$

r representing the radius of the streamtube.

In climb, the relation $w = 2v$ can be shown to remain valid in momentum theory. Figure 2.1 illustrates the flow field for an actuator disk in climb.

As such, the thrust developed by a rotor in climbing flight is

$$T = 2\rho A(V + v)v. \tag{2.21}$$

Substituting 2.11 into the previous equation, the variation of the induced velocity v with climb speed is found:

$$v = -\frac{V}{2} + \sqrt{\left(\frac{V}{2}\right)^2 + v_{Hover}^2} > v_{Hover}. \tag{2.22}$$

The induced velocity required to maintain constant thrust in climb is shown to rise. This translates to a rise in the minimum required power in climb, as shown by

$$P = T\left(\frac{V}{2} + \sqrt{\left(\frac{V}{2}\right)^2 + v_{Hover}^2}\right) > T\left(V + v_{Hover}\right). \tag{2.23}$$

This section has shown that momentum theory can be used to determine the theoretical limits of rotor performance. While the precision of the results is limited by the assumptions required to use the model, these results can be used as a form of verification for other models. The analytical form of the theory permits very fast calculation time as well. There exist a number of extensions to momentum theory that can increase the fidelity of the results. Common variations include :

- varying the induced velocity along the blade span ($v = v(r)$) instead of using an average velocity;
- adding a swirl velocity in the wake of the rotor;
- adding profile drag from a lookup table for better power requirement prediction;
- coupling momentum theory to blade element theory.

Increasing the model's fidelity will only serve to increase the induced power requirement.

2.2 Blade Element Theory

While momentum theory provides a general design space for helicopter performance, it lacks a large number of details in its results, especially the distribution of the aerodynamic loading on the helicopter blades. Blade Element Theory seeks to remedy this limitation by extending

Prandtl's lifting-line method to rotating wings. The assumptions to the most basic form of Blade Element Theory are :

- each 2D airfoil section on a blade is independent from the rest of the blade;
- 2D sectional lift coefficient c_l is known;
- 2D sectional drag coefficient c_d is known.

Figure 2.2 shows the basic geometric relations and notations used in Blade Element Theory. The lift and drag generated by a 2D airfoil of chord length c are

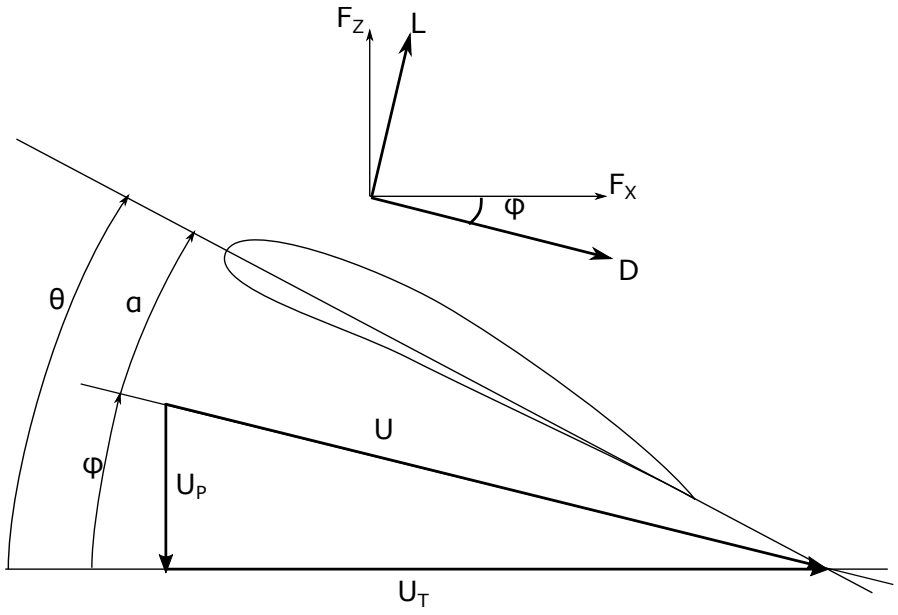

Figure 2.2 Momentum Theory in Climb

$$L_{2D} = \frac{1}{2}\rho U^2 c_l c, \tag{2.24}$$

$$D_{2D} = \frac{1}{2}\rho U^2 c_d c, \tag{2.25}$$

where the lift is perpendicular to the freestream velocity U, and the drag is parallel to it. The lift and drag are reoriented to obtain a force perpendicular to the rotor disk plane (thrust) and parallel to it. The perpendicular component is the thrust generated by the rotor and the parallel component is multiplied by its distance to the rotor hub (centre of rotation) r to

obtain the drag torque :

$$T_{2D} = F_z = L_{2D}\cos\varphi - D_{2D}\sin\varphi \tag{2.26}$$

$$Q_{2D} = F_x r = \left(L_{2D}\sin\varphi + D_{2D}\cos\varphi\right) r \tag{2.27}$$

To obtain the total quantities of the thrust and torque on a rotor blade, these quantities must be integrated along the rotor span :

$$T = \int_{r_i}^{R_{Tip}} \left(\frac{1}{2}\rho U(r)^2 c_l c(r)\cos\varphi - \frac{1}{2}\rho U(r)^2 c_d c(r)\sin\varphi\right) dr, \tag{2.28}$$

$$Q = \int_{r_i}^{R_{Tip}} \left(\frac{1}{2}\rho U(r)^2 c_l c(r)\sin\varphi + \frac{1}{2}\rho U(r)^2 c_d c(r)\cos\varphi\right) r dr. \tag{2.29}$$

For rotating wings, the tangential velocity U_T, created by the rotating motion of the blade, varies along the blade span. For a rotor in axial flight, this is given by $U_T(r) = \Omega r$. The component of the velocity perpendicular to the rotor disk U_P is obtained with the climb speed and the induced velocity ($U_P = V_{Climb} + v_{Induced}$). Generally, the flow angle $\varphi = \arctan\frac{U_P}{U_T}$ is small, because $U_T >> U_P$. Therefore, the small angle assumption may be used ($\cos\varphi \approx 1, \sin\varphi \approx \varphi$). Furthermore, if stall and compressibility effects are neglected, $c_\ell = c_{\ell 0} + a\alpha \approx c_{\ell 0} + a\left(\theta - \frac{U_P}{U_T}\right)$. Combining these assumptions, one obtains

$$T = \int_{r_i}^{R_{Tip}} \frac{1}{2}\rho U_T(r)^2 \left(c_{\ell 0} + a\left(\theta - \frac{U_P}{U_T}\right) c(r)\right) dr, \tag{2.30}$$

$$Q = \int_{r_i}^{R_{Tip}} \left(\left(\frac{1}{2}\rho U_T(r)^2 \left(c_{\ell 0} + a\left(\theta - \frac{U_P}{U_T}\right) c(r)\right)\right)\phi + \frac{1}{2}\rho U(r)^2 c_d c(r)\right) r dr. \tag{2.31}$$

While such simplifications allow for analytical integration, the efficiency of modern day processors permits the numerical integration of the non-linear form of these equations with a high degree of accuracy.

As previously stated, Momentum Theory may also be integrated into Blade Element Theory to compute the previously neglected induced velocity $v_{induced}$. For an infinitely thin annulus, Momentum Theory gives

$$dT = 4\pi\rho\left(V_{Climb} + v_{Induced}\right) v_{Induced} r dr. \tag{2.32}$$

The value of $v_{Induced}$ can therefore be obtained iteratively or, with simplifying assumptions,

be calculated analytically.

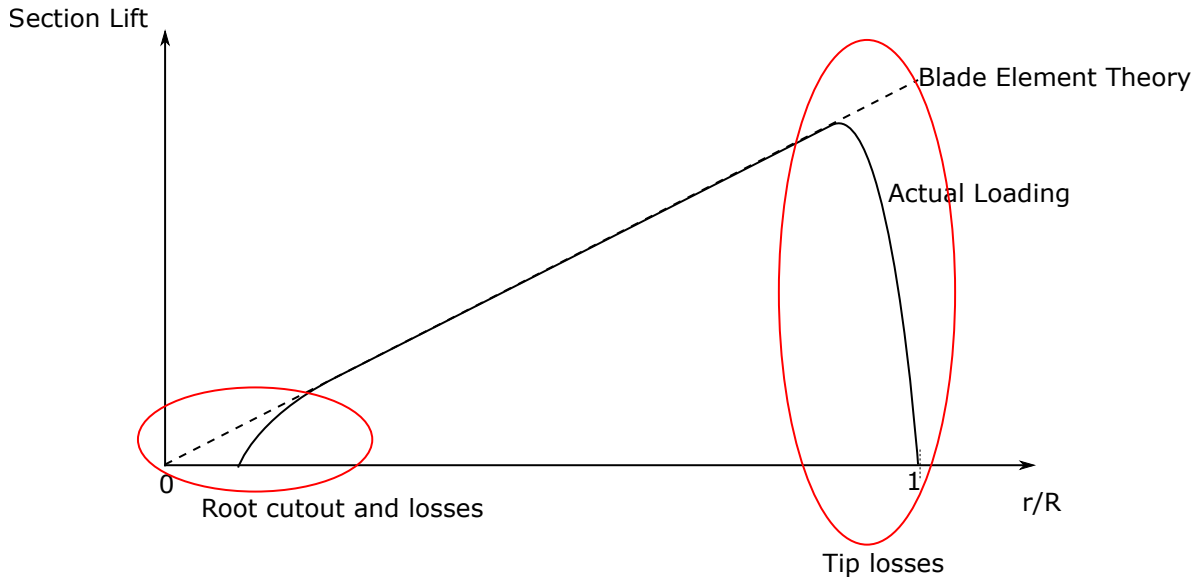

Figure 2.3 Effect of Tip and Root Loss of Lift

While the combined model of Blade Element Theory and Momentum Theory accesses a higher degree of fidelity, there are still certain physical inaccuracies in the results. Of notable importance is the lack of blade root and tip losses (see figure 2.3). This is one of the principal drawbacks of Blade Element Momentum Theory, in that we lose the effect of the wake on the blade performance. Furthermore, flow unsteadiness is not modelled. There are many models that may be added to Blade Element Theory to correct this issue. These models may be as simple as empirical or heuristic modifications to the lift distribution. Other models include the effects of wake distribution in the fluid domain. The reader is referred to the works of Johnson (2012) and Stepniewski and Keys (1979) for further detail.

2.3 Models Based on the Biot-Savart Equation

The assumptions made for Momentum Theory and Blade Element Theory limits their physical accuracy. In particular, the disregard of the effect of the rotor wake disadvantages the models in dynamic situations. The wake generated by a lifting surface can be seen as extremely vortical in nature. Assuming potential flow (see section 1.1.1), the Biot-Savart equation may be used to describe the velocity around a vortex. The basic form of the Biot-Savart equation, as defined in Katz and Plotkin (2001) and reformulated in Conlisk (2001),

is

$$\vec{U}_V = -\frac{1}{4\pi}\int \frac{\left(\vec{X}-\vec{X}'\right)\times\vec{\omega}}{\left\|\left(\vec{X}-\vec{X}'\right)\right\|^3}dV'. \tag{2.33}$$

In essence, the velocity $\vec{U}_V$ induced by a vortex filament on a point $\vec{X}$ is a function of the distance between the two elements $\left\|\left(\vec{X}-\vec{X}'\right)\right\|$, the vortex filament's "view" on the point of interest and the strength of the vortex filament. The equation integrates over the volume of the vortex filament. The vorticity of the infinitesimal volume dV' located at point $\vec{X}'$ is given by $\vec{\omega}$.

Models based upon the Biot-Savart equation come in many forms. They can be decomposed into three main components: blade representation, wake representation and wake development. There exist a certain number of solutions for each component. These components can be considered as independent and may be combined as required (Conlisk, 2001).

2.3.1 Blade Modelling

Two methods are predominant in modelling lifting surfaces using the Biot-Savart equation: Lifting Line methods and panel methods. In both cases, the blade is discretized into i subelements that produce circulation of strength Γ_i. The force produced is associated to this circulation strength, as defined by

$$\vec{F} = \rho\left(\vec{U}_\infty + \vec{U}_{Body}\right)\times\vec{\Gamma}_i. \tag{2.34}$$

These circulation-based elements shed their vorticity into the freestream, satisfying Kelvin's theorem. The wake produces a downwash or upwash on these subelements, thereby modifying their angle of attack and their generated lift.

Lifting Line methods represent rotor blades as vortex filaments. This method may be viewed as blade-element theory with the addition of wake effects. The lift generated by the blade is determined by coupling each subelement to a lift curve, be it to the simple $C_L = 2\pi\alpha$ assumption, or to a full 2D viscous database.

Panel methods represent either the camberline of the blade or the blade surface. This allows the effect of blade camber to be taken into account without the use of a 2D viscous database. However, Parenteau (2017) has shown that coupling panel methods to a viscous 2D database may be beneficial when modelling lifting surfaces in post-stall regions.

2.3.2 Wake Development

Three methods of propagating the wake behind lifting surfaces have been identified: the prescribed/rigid wake, the free wake and the relaxed wake. Each method is described in this section, along with an example for each method.

Prescribed/Rigid Wake

The prescribed or rigid wake is the simplest and least computationally expensive wake model. The geometry of the wake is described using analytical, empirical, semi-empirical or heuristic equations.

For rotor wakes, the simplest heuristic model generates a helicoidal wake issued from each blade's trailing edge. More advanced models, such as that presented in Landgrebe (1972), may take into account that the inboard wake descends more rapidly than the outboard wake. These models often depend on the thrust generated by the helicopter rotor.

Young (1974) presents Landrgrebe's prescribed wake model for hovering rotors. This model uses five equations to describe the rotor wake:

- tip vortex axial travel;
- tip vortex radial travel;
- inboard sheet ($\bar{r} = \frac{r}{R} = 0$) vortex axial travel;
- outboard sheet ($\bar{r} = \frac{r}{R} = 1$) vortex axial travel;
- sheet vortex radial position.

The tip vortex is placed using the following equations (noting that $\psi_b = 360\,\mathrm{deg}\,/N$, N being the number of blades in the rotor):

$$\bar{z}_{tip} = \begin{cases} K_1\psi & 0 \leq \psi \leq \psi_b \\ K_1\psi_b + K_2\left(\psi - \psi_b\right) & \psi > \psi_b \end{cases} \tag{2.35}$$

where

$$K_1 = -0.25\left(\frac{C_T}{\sigma} + 0.001\theta_1\right) \tag{2.36}$$

$$K_2 = -\left(1.41 + 0.0141\theta_1\right)\sqrt{\frac{C_T}{2}}, \tag{2.37}$$

θ_1 is the blade linear twist, in degrees and $\sigma = \frac{A_{Blades}}{A_{Disk}} = \frac{Nc}{\pi R}$ is the blade solidity.

$$\bar{r}_{tip} = 0.78 + 0.22e^{-\lambda\psi} \tag{2.38}$$

with

$$\lambda = 0.145 + 27.0C_T \tag{2.39}$$

The vortex sheet's axial position varies linearly between the following equations :

$$\bar{z}_{\bar{r}=0} = \begin{cases} 0 & 0 \leq \psi \leq \frac{\pi}{2} \\ K_{20}\left(\psi - \frac{\pi}{2}\right) & \psi > \frac{\pi}{2} \end{cases} \tag{2.40}$$

$$\bar{z}_{\bar{r}=1} = \begin{cases} K_{11}\psi & 0 \leq \psi \leq \psi_b \\ K_{11}\psi_b + K_{21}\left(\psi - \psi_b\right) & \psi > \psi_b \end{cases} \tag{2.41}$$

where

$$K_{20} = \frac{\theta_1}{128.0}\left(0.45\theta_1 + 18.0\right)\sqrt{\frac{C_T}{2}} \tag{2.42}$$

$$K_{11} = -2.2\sqrt{\frac{C_T}{2}} \tag{2.43}$$

$$K_{21} = -2.7\sqrt{\frac{C_T}{2}}. \tag{2.44}$$

The vortex sheet's radial location can be found using

$$\bar{r} = \bar{r}_{release}\bar{r}_{tip}, \tag{2.45}$$

where $\bar{r}_{release}$ refers to the radial position on the rotor where the vortex filament originated from.

Figure 2.4 shows the result of using the Young wake model for a two-bladed rotor (one rotor shown) with $C_T = 0.0070, \sigma = 0.02$. It can be seen that the tip vortex travels downwards (axially) at a slower rate than the inner sheet. This is due to the relative strength of the tip vortex in relation to the inner sheet; the tip vortex is much larger and influences the panels near it to a greater extent than the inner panels may influence the tip vortex. As such, the wake develops into a cone shape as it ages.

As noted previously, this prescribed wake model (as well as many others) has a dependency on the thrust generated by the rotor. An iterative method is therefore required to determine the thrust generated by a helicopter rotor. The algorithm in figure 2.5 is used to determine

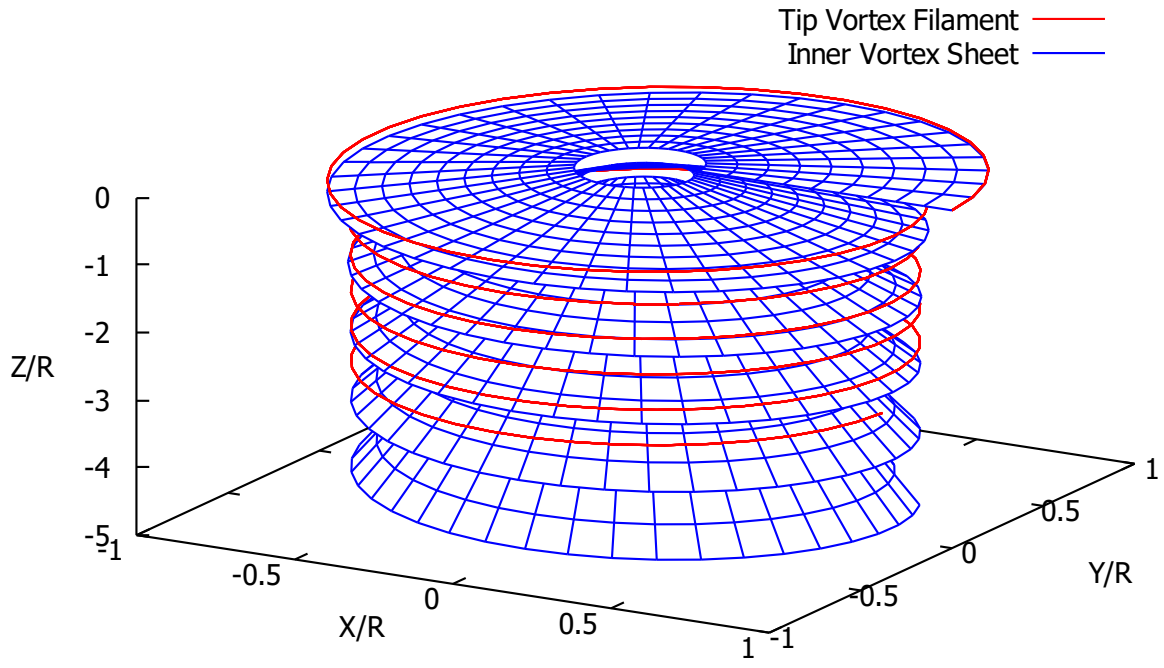

Figure 2.4 Young Prescribed Wake Model

the rotor's thrust coefficient. One simply needs to determine the number of wake elements to place in the flowfield. Using a prescribed wake to converge on the thrust generated by a helicopter rotor is characteristically stable and converges rapidly.

The first pass in the algorithm calculates the thrust generated by the rotor if there was no wake. The thrust is then used to generate the shape of the wake. The circulation on the trailing edge of each blade is then propagated through the wake. This process is repeated until the thrust calculation converges. Overestimating the thrust coefficient will lead to the underestimation of C_T at the following iteration. Similarly, an underestimated thrust coefficient leads to an overestimated C_T at the next iteration. If one were to display the wake geometry at every iteration of the algorithm, the wake would have a motion similar to that of an overdamped spring-mass system. While not necessary, the use of a carefully chosen relaxation factor may reduce the number of iterations required to reach convergence. Convergence is typically reached within 10 iterations without the use of a relaxation factor.

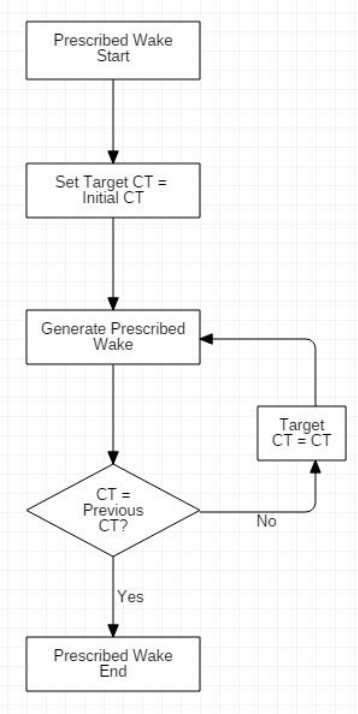

Figure 2.5 Prescribed Wake Convergence Algorithm

Free Wake

The free wake model is a computationally expensive model where the wake is convected with the flowfield velocity. This method is also more physically accurate, as it captures complex wake effects, such vortex rollup. It also increases the precision of wake effects for dynamic control inputs.

The wake is moved at each calculated iteration using a time-stepping scheme. The Adams Methods are of particular interest, as they provide flexibility in the solution's order of accuracy. The Adams-Bashforth method is the explicit scheme, while the Adams-Moulton method is an implicit scheme (Quarteroni *et al.*, 2010).

The Adams methods are defined by the following equation :

$$\vec{x}_{n+s} = \vec{x}_{n+s-1} + \Delta t \sum_{j=p}^{s} b_{n+s-j} \vec{U}_{n+s-j}. \tag{2.46}$$

The Adams-Bashforth scheme is obtained when $p = 1$ and is accurate to s^{th} order. Note that if $s = 1$, the explicit Euler scheme is obtained. The b coefficients can be obtained with the

following equation :

$$b_{s-k-1} = \frac{(-1)^k}{i!\,(s-k-1)!} \int_0^1 \prod_{i=0, i\neq k}^{s-1} (u+i)\, du, \tag{2.47}$$

for $k = 0$ to $s-1$. The Adams-Moulton scheme is obtained when $p = 0$ and is accurate to the $(s+1)^{th}$ order. The b coefficients can be obtained with the following equation :

$$b_{s-k} = \frac{(-1)^k}{k!\,(s-k)!} \int_0^1 \prod_{i=0, i\neq k}^{s-1} (u+i-1)\, du \tag{2.48}$$

for $k = 0$ to s.

The drawback of the Adams-Moulton scheme is that solving the implicit equation is computationally expensive. To reduce computational cost while maintaining a higher order of precision, the Adams-Bashforth-Moulton predictor-corrector scheme may be used. This scheme begins by calculating the predicted final position $\vec{x}'_{n+s}$ using the Adams-Bashforth scheme. Another Adams-Bashfort step is then calculated, replacing $\vec{U}_{n+s}$ by $\vec{U}'_{n+s}$, the velocity calculated at the predictor point. While this method is more computationally efficient than the Adams-Moulton scheme, the required computational cost is still twice that of the Adams-Bashforth method. This scheme is, however, "known to be more stable than the conventional explicit method for the wake roll-up" (Wie *et al.*, 2009).

Figure 2.6 shows a sample output of a Vortex-Lattice Method with panel free-wake using the explicit Euler scheme. As stated previously, the free-wake methodology allows the development of physical phenomena that could otherwise be neglected or filtered by other wake propagation methods. Note how the deformation calculated in the free-wake methodology allows the formation of tip vortices and the coning of the wake. An advantage of the UVLM is also visible in this figure; the lift distribution (proportional to Γ) accounts for the effects of rotor tip and root cutout losses.

Relaxed Wake

The relaxed wake can be viewed as a compromise between the prescribed wake and the free wake. The wake is assumed to be periodically stable and that it may reach a steady-state solution. Starting from an initial wake distribution and enforcing the periodicity condition, the position of the wake is solved iteratively until it is relaxed into its steady-state position. As explained in Conlisk (2001), the position of the wake element is written as a function of two variables and is derived in time,

$$\frac{d\vec{x}}{dt} = \frac{\partial \vec{x}}{\partial t} + \frac{\partial \vec{x}}{\partial \alpha}\frac{d\alpha}{dt} \tag{2.49}$$

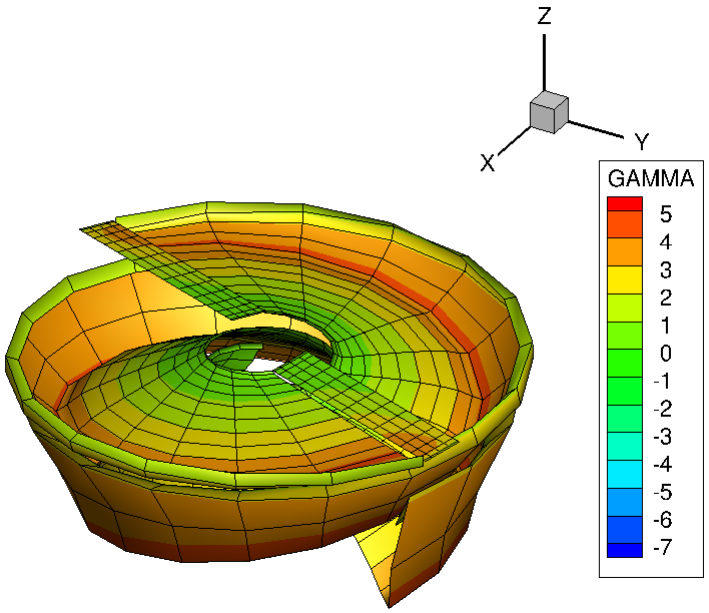

Figure 2.6 Wake Development Using the Free-Wake Methodology

The wake age ζ is defined as the azimuthal distance the rotor has travelled Ψ since the wake element has been shed. The time variable may be written as a function of wake age $t = \zeta/\Omega$. The variable α may also be written as a function of azimuthal angle $\alpha = \Psi/\Omega$. If the variables ζ and Ψ grow at the same rate, $\frac{d\alpha}{dt} = 1$. Spatial periodicity is assumed, therefore

$$\vec{x}\left(\Psi, \zeta\right) = \vec{x}\left(\Psi + 2\pi, \zeta\right). \tag{2.50}$$

In other words, two wake elements shed from the same location, but at different instances in time, will move along the same path as they age.

The position equation of a wake element can therefore be rewritten as

$$\frac{\partial \vec{x}}{\partial \zeta} + \frac{\partial \vec{x}}{\partial \Psi} = \frac{\vec{U}}{\Omega}, \tag{2.51}$$

which is the one-dimensional wave equation for forward transporting properties. If equation 2.51 is discretized with forward differencing in time (ζ) and central differencing in space (Ψ),

the following equation is obtained :

$$\frac{\vec{x}\left(\Psi,\zeta+\Delta\zeta\right)-\vec{x}\left(\Psi,\zeta\right)}{\left(\zeta+\Delta\zeta\right)-\left(\zeta\right)}+\frac{\vec{x}\left(\Psi+\Delta\Psi,\zeta\right)-\vec{x}\left(\Psi-\Delta\Psi,\zeta\right)}{\left(\Psi+\Delta\Psi\right)-\left(\Psi-\Delta\Psi\right)}=\frac{\vec{U}}{\Omega} \tag{2.52}$$

$$\vec{x}\left(\Psi,\zeta+\Delta\zeta\right)=\vec{x}\left(\Psi,\zeta\right)+\frac{\vec{U}\Delta\zeta}{\Omega}-\frac{\vec{x}\left(\Psi+\Delta\Psi,\zeta\right)-\vec{x}\left(\Psi-\Delta\Psi,\zeta\right)}{2} \tag{2.53}$$

$$\vec{x}\left(\Psi,\zeta+\Delta\zeta\right)=\vec{x}\left(\Psi,\zeta\right)+\frac{\vec{U}\Delta\zeta}{\Omega}-\frac{\vec{x}\left(\Psi+\Delta\Psi,\zeta\right)-\vec{x}\left(\Psi+2\pi-\Delta\Psi,\zeta\right)}{2} \tag{2.54}$$

There is a great similarity to the backward Euler time integration method, as defined by

$$\vec{x}(t+\Delta t)=\vec{x}(t)+\vec{U}\Delta t \tag{2.55}$$

In fact, the second term on the right-hand side of equation 2.54 can be rewritten as $\vec{U}\Delta t$. The third term of the right-hand side of the same equation can therefore be seen as a correction term to the convection equation. This equation is applied to the wake iteratively until the solution has converged (i.e. the wake is free of motion). This discretization scheme is rather simple and may lead to numerical instability. Bagai and Leishman (1995) present improved and stable discretization schemes that are better suited to the task. This method of displacing the wake is not developed further in this work.

2.3.3 Wake Representation

Three wake representations are presented : the panel wake, the continuous vorticity contour wake and the vortex particle (vorton) wake.

Panel Wake

The panel wake is represented as a lattice of vortex elements, as was presented in figure 1.1. This model is the Vortex-Lattice Method's most common representation of the wake, as defined by Katz and Plotkin (2001). Each wake panel is created at the trailing edge of the lifting surface as to enforce the zero circulation "Kutta Condition" (Anderson Jr, 2010) at the trailing edge. In other words, the circulation strength Γ of the wake panel shed at the trailing edge is equal to the strength of the trailing edge panel.

The wake panel is represented as a vortex ring. Four straight-line vortex elements (SLVE) are positioned using four control points at the corners of the ring. When placed in a lattice, adjacent vortex rings share an SLVE. As such, the evaluation of the Biot-Savart equation on these SLVEs need only be calculated once, replacing the circulation strength by the

circulation differential $\Delta\Gamma$ between adjacent panels.

Multiple methods exist for the evaluation of position updates of the control points in the free-wake methodology. The simplest is to evaluate the velocity at the control point itself. Another method requires the evaluation of the velocity at the centre of each SLVE. The control point is then displaced at the average velocity of its neighbouring SLVEs. The stretching of the SLVEs is inherently calculated with the displacement of its control points. The stretching of a vortex filament also affects its circulation strength. This topic will be discussed in section 3.1.4.

Continuous Vorticity Contour Wake

The Continuous Vorticity Contour (CVC) model, developed by Continuum Dynamics Inc. (Quackenbush *et al.*, 1990) was developed to reduce the computational requirements for a free-wake model. After a pre-defined number of iterations, the shed wake panels of strength Γ_i are replaced by vortex filaments of predetermined strength $\Delta\Gamma$. These filaments are placed along the trailing wake panel so as to contain $\Delta\Gamma$ circulation between each filament (see figure 2.7). The curve in the previous figure is obtained by integrating each panel's Γ, noting that the cumulated circulation is zero at the rotor tip and hub. In order to respect the Kutta condition (zero circulation on the trailing edge), vortex filaments cannot be shed directly from the lifting surface. A buffer consisting of panel elements in the wake is required to transition to the CVC wake model. In rotorcraft, this transition is suggested to be made after 1 rotor revolution (Quackenbush *et al.*, 1990).

Figure 2.8 shows how the CVC wake would develop for a rotor in high-speed flight. The CVC model allows the creation of self-contained loops of vorticity. This wake model visually represents a contour map of vorticity in the wake. Figure 2.9 shows the wake developed for a rotor blade in hover. As expected the vortex lines near the rotor tip are closely spaced together, indicating a large and rapid decrease in generated lift near the rotor tip. The same is noted near the rotor hub, but to a lesser extent, due to the generated lift being much weaker at the slower moving blade root.

By selecting a sufficiently large value for $\Delta\Gamma$, the number of elements evaluated in the wake can be significantly decreased. Coupled with a fast panel solver method (Quackenbush *et al.*, 1990) and by limiting the number of wake elements, this method could achieve real-time simulation speeds (Horn *et al.*, 2006).

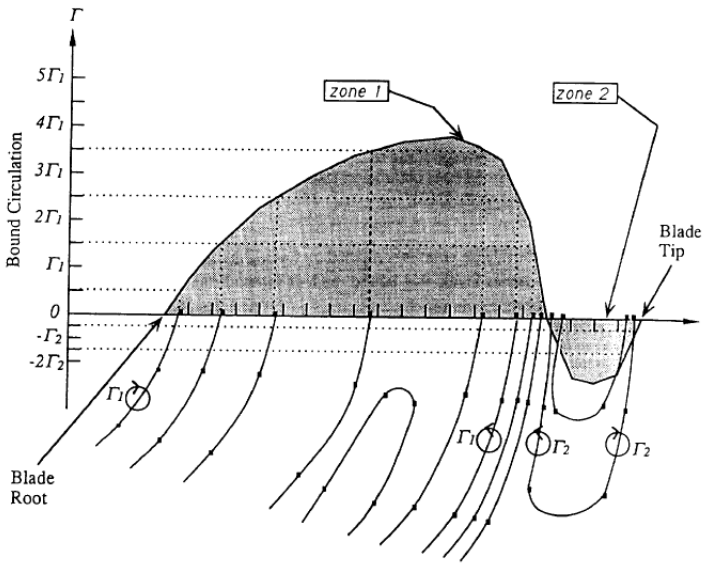

Figure 3-8. Radial bound circulation distribution for a rotor with positive and negative circulation zones, showing the release points of trailing wake filaments.

Γ_1 = filament strength in zone 1

Γ_2 = filament strength in zone 2

Figure 2.7 CVC Wake Release Points (Quackenbush *et al.*, 1990)

Vortex Particle Wake

This wake model is different from the previous wake models in that vortices are no longer represented as filaments. The wake is instead represented as infinitesimal vortex particles (or vortons), represented by their position $\vec{x}$ and a circulation vector $\vec{\Gamma}$. This method lends itself particularly well to acceleration techniques, such as multipole algorithms (Lindsay and Krasny, 2001). Such techniques have been successfully implemented in both fixed-wing aircraft (Willis *et al.*, 2007) and rotorcraft (Tan and Wang, 2013). However, there is additional computational overhead associated to this method. This is due to the need to calculate the deformation (or strain) of the vorticity vector. Whereas this is calculated in the motion of a vortex filament, the infinitesimal size of the vorton requires the calculation of the velocity gradient at its location to properly determine the strain of the vorticity vector. This method will be presented in further detail in section 3.2.1. Figure 2.10 shows a sample output of a Vorton wake using free-wake convection.

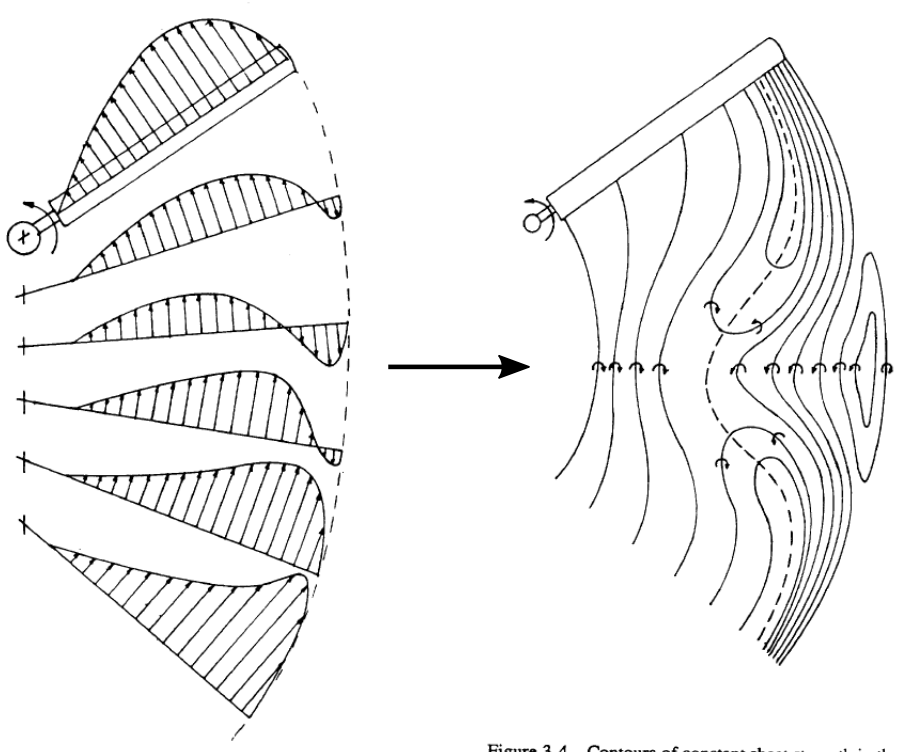

Figure 3-3. Typical load variations on the advancing side in high speed flight.

Figure 3-4. Contours of constant sheet strength in the wake on the advancing side.

Figure 2.8 CVC Wake Illustration (Quackenbush *et al.*, 1990)

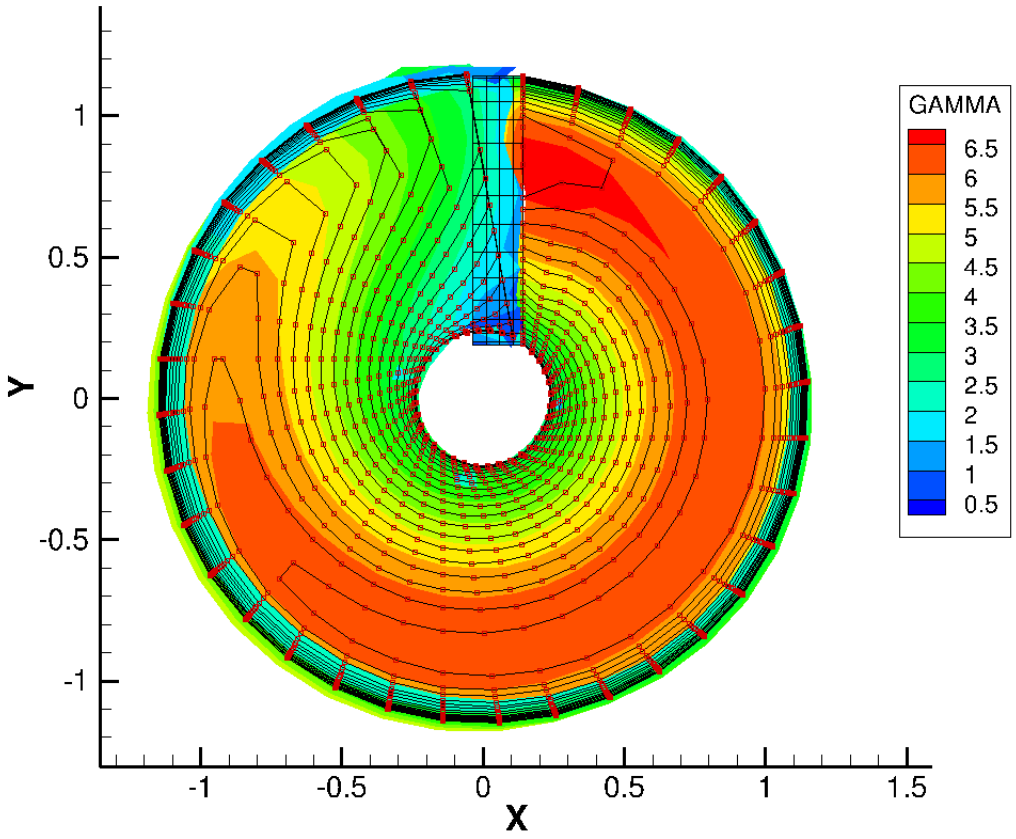

Figure 2.9 CVC Wake Vorticity Distribution for One Rotor Rotation

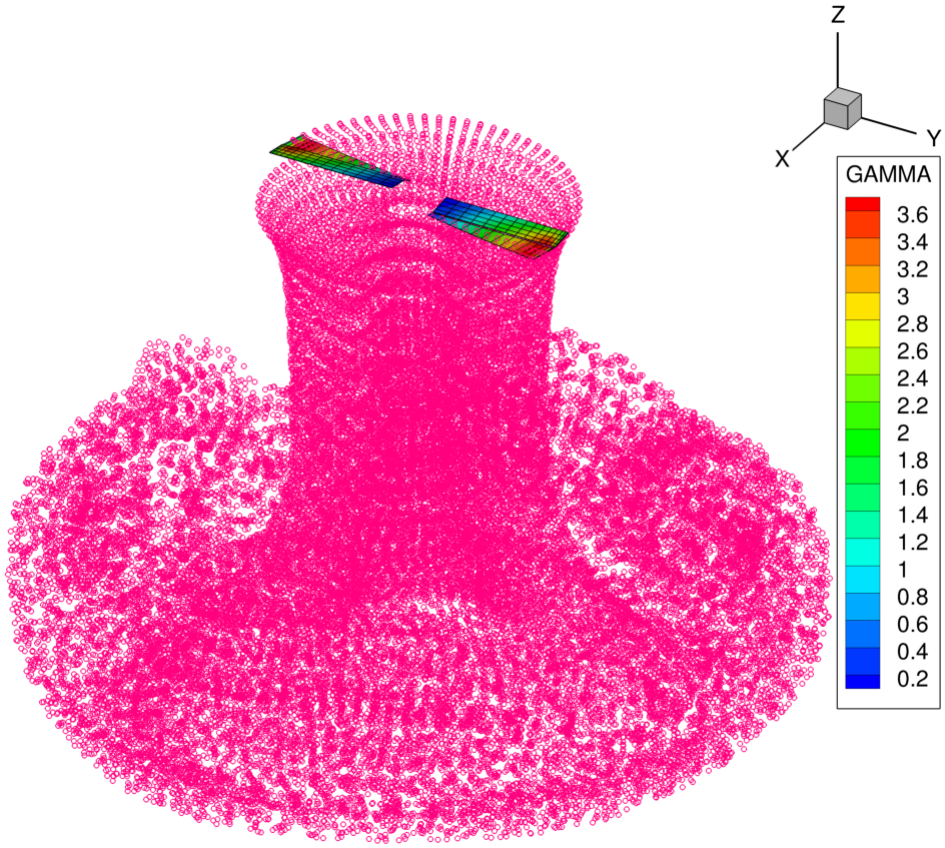

Figure 2.10 Vortex Particles after 10 Rotor Rotations Convected Using Free-Wake

2.4 Grid-Based Models

Grid-based models solve the discretized Continuity, Navier-Stokes and Energy equations in a Favre-averaged manner (Blazek, 2005), consisting of writing the field Ψ as the sum of a mean component $\bar{\Psi}$ and a fluctuating component Ψ'. In their conservative forms, these equations are :

$$\frac{D\rho}{Dt} = 0, \tag{2.56}$$

$$\frac{D(\rho u)}{Dt} = -\frac{\partial p}{\partial x} + \nabla \cdot (\mu \nabla u) + S_x, \tag{2.57}$$

$$\frac{D(\rho v)}{Dt} = -\frac{\partial p}{\partial y} + \nabla \cdot (\mu \nabla v) + S_y, \tag{2.58}$$

$$\frac{D(\rho w)}{Dt} = -\frac{\partial p}{\partial z} + \nabla \cdot (\mu \nabla w) + S_z, \tag{2.59}$$

$$\frac{D(\rho e)}{Dt} = -p\nabla \cdot \vec{U} + \nabla \cdot (k \nabla T) + \Phi + S_e, \tag{2.60}$$

where viscous stress terms are incorporated in the S_x, S_y, S_z, S_i and Φ variables. There are various methods in solving these equations, such as the finite difference approach (Cebeci *et al.*, 2005), the finite volume approach (Versteeg and Malalasekera, 2007) and finite element approach (Anderson and Wendt, 1995). The commonality between these methods is that they all require a discretization of the fluid domain into a grid (mesh) to solve the partial differential equations numerically. In the aerospace community, turbulence is often modelled using the Boussinesq assumption (Blazek, 2005)

$$\mu_T = \epsilon \frac{\partial u}{\partial y} \tag{2.61}$$

so that

$$\mu = \mu_L + \mu_T, \tag{2.62}$$

μ_L being the laminar viscosity of the fluid and μ_T being the turbulent viscosity.

It is important to note that solving these equations in their discretized form leads to numerical dissipation and/or dispersion errors. To reduce this error, high-order schemes and/or refined meshes are required, increasing computational cost and model complexity. Derived parameters, such as vorticity, are greatly affected by these errors. In the case of rotorcraft, the rotor wake may be diffused after two rotor rotations, thus affecting the pressure distribution around the rotor blades. Hariharan *et al.* (2015) present the characteristics of seven CFD solvers being developed for helicopter performance prediction.

Alternatively, the momentum equations may be rewritten to include a "vorticity confinement" term allowing vortical structures to be solved and conserved (Steinhoff and Underhill, 1994). In essence, the vorticity confinement equations provide a negative diffusion factor in regions of strong vorticity. Flow vorticity is thus conserved over much greater distances. Costes and Kowani (2003) presents the potential benefits of the method.

Another approach to conserving wake vorticity while decreasing computational cost is to use a hybrid grid-based/Lagrangian solver. These models solve the flow around rotor blades using a grid-based approach. Wake elements (filaments or particles, for example) are then released from the blade at the vorticity centroid (Egolf *et al.*, 2010). The wake elements may then be convected using a free-wake methodology, using the velocity calculated by the grid-based solver (Rajmohan, 2010). These wake elements also affect the flow solution through the addition of source terms in the grid-based solver. Grid based methods fall outside the scope of this study.

2.5 Summary

This chapter presented a literature review of the current methods employed in the field of helicopter aerodynamics. Low fidelity models, such as Momentum Theory and Blade Element Theory were presented. Low to medium fidelity models using the Biot-Savart equation to model vorticity were then shown. High fidelity models, such as RANS simulations, were also briefly explained.

CHAPTER 3 DEVELOPMENT OF THE UVLM

This chapter presents the theory behind the implementations made to the classic UVLM. In order to remove the numerical singularity of the Biot-Savart equation, two viscous core models are implemented: the Lamb-Oseen core model and the Vatistas core model. The numerical instabilities found in ground effect are also explained. To attenuate these instabilities, the vortex-particle wake was implemented.

3.1 Viscous Core Models

3.1.1 Basic Principles

The Biot-Savart Law is a solution to Laplace's equation. The velocity at point $\vec{P}$ induced by an arbitrary vortex filament, as illustrated in figure 3.1 is calculated as follows :

$$\vec{u} = \frac{1}{4\pi} \int_C \Gamma \frac{d\vec{l} \times \vec{r}}{\|\vec{r}\|^3}. \tag{3.1}$$

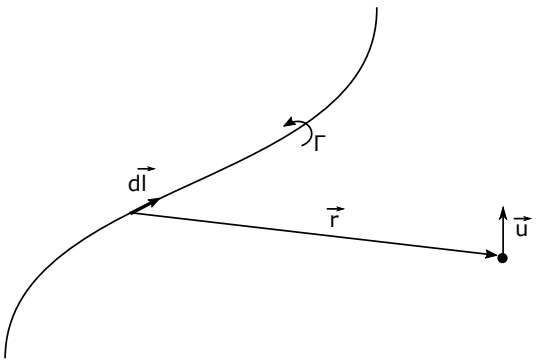

Figure 3.1 Notation for an arbitrary Straight-Line Vortex Element

Consider the case where the vortex element is represented by a straight line with constant

circulation Γ along its length. Using the notation in figure 3.2, as shown in Katz and Plotkin (2001), the induced velocity is calculated as

$$u = \frac{\Gamma}{4\pi r} \left(\cos \beta_1 - \cos \beta_2 \right), \tag{3.2}$$

with β_i being the angle between $\vec{r}_0$ and $\vec{r}_i$. The velocity $\vec{u}$ at point $\vec{P}$ is perpendicular to the

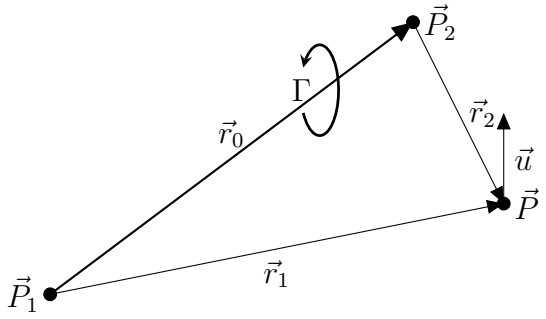

Figure 3.2 Biot-Savart Law for Finite Length Line Segment

plane created by the straight-line vortex element (SLVE) and $\vec{P}$ and is oriented following the right-hand rule around the vortex segment. Consider the following relations :

$$r = \frac{\|\vec{r}_1 \times \vec{r}_2\|}{\|\vec{r}_0\|} \tag{3.3}$$

$$\cos \beta_1 = \frac{\vec{r}_0 \cdot \vec{r}_1}{\|\vec{r}_0\| \, \|\vec{r}_1\|} \tag{3.4}$$

$$\cos \beta_2 = \frac{\vec{r}_0 \cdot \vec{r}_2}{\|\vec{r}_0\| \, \|\vec{r}_2\|} \tag{3.5}$$

$$\vec{e}_\theta = \frac{\vec{r}_1 \times \vec{r}_2}{\|\vec{r}_1 \times \vec{r}_2\|} \tag{3.6}$$

Substituting these equations into equation 3.2, one obtains

$$\vec{u} = u\vec{e}_\theta = \frac{\Gamma}{4\pi} \frac{\vec{r}_1 \times \vec{r}_2}{\|\vec{r}_1 \times \vec{r}_2\|^2} \vec{r}_0 \cdot \left(\frac{\vec{r}_1}{\|\vec{r}_1\|} - \frac{\vec{r}_2}{\|\vec{r}_2\|} \right). \tag{3.7}$$

When the straight-line vortex element is stretched to infinity in both directions (2D approximation), the values of $\cos \beta_1$ and $\cos \beta_2$ go to 1 and -1, respectively. Therefore, a 2D vortex filament's induced velocity is given as

$$u = \frac{\Gamma}{2\pi r}, \tag{3.8}$$

which is a simple function of the distance r of point $\vec{P}$ from the vortex filament. This equation exhibits a singularity as r approaches 0, as demonstrated by figure 3.3.

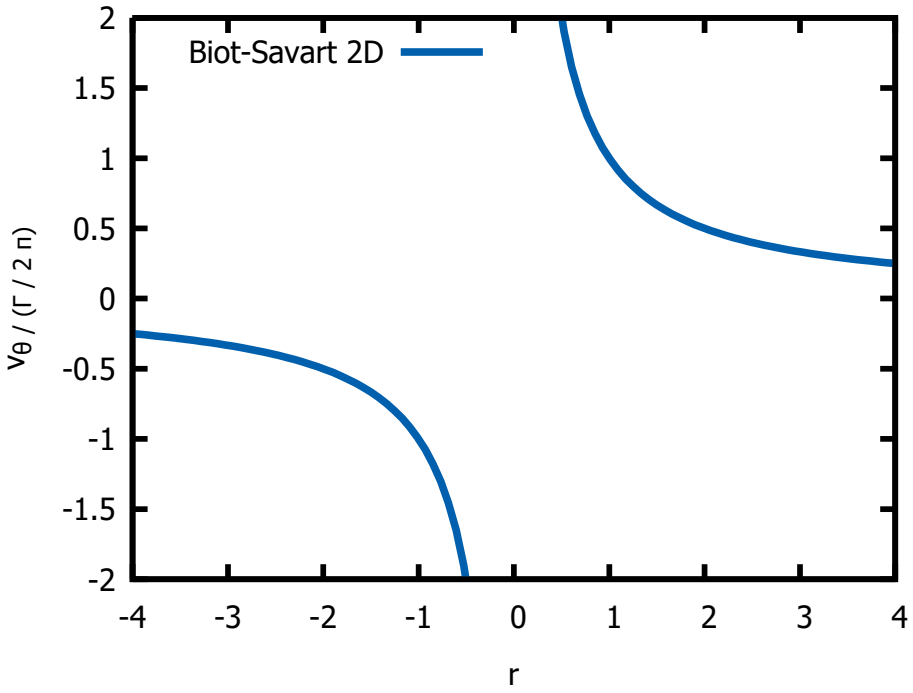

Figure 3.3 The 2D Biot-Savart Equation

Such a form of the Biot-Savart law can lead to numerical instability in the VLM, where a particle approaching the vortex filament would be subjected to uncharacteristically large velocities that may lead to numerical error. Such a velocity jump could not be sustained in a real fluid, where viscosity would lead to the smoothing of the velocity field around the vortex filament. Two viscous core models, the Lamb-Oseen core model and the Vatistas core model, are presented in the following sections to remove the numerical singularity in the Biot-Savart Law. A third core model, the Scully core model, will be used in section 4. It is obtainable through the Vatistas formulation, as will be shown in section 3.1.3.

3.1.2 The Lamb-Oseen Core Model

The Lamb-Oseen Core Model is obtained by solving the Navier-Stokes equations in its laminar formulation in one dimension (Leishman *et al.*, 2002). The velocity profile for a two-

dimensional filament using the Lamb-Oseen core model is given by

$$u = \frac{\Gamma}{2\pi r}\left(1 - e^{-\frac{r^2}{4\nu t}}\right), \tag{3.9}$$

where ν is the static viscosity and t is time. The size of the viscous core is defined as the point where the velocity is maximized. To determine the viscous core size r_c, u is differentiated with respect to r. The velocity is maximized when $du/dr = 0$.

$$\left.\frac{du}{dr}\right|_{r=r_c} = -\frac{\Gamma}{2\pi r_c^2}\left(1 - e^{-\frac{r_c^2}{4\nu t}}\right) + \frac{\Gamma}{4\pi\nu t}e^{-\frac{r_c^2}{4\nu t}} = 0 \tag{3.10}$$

By imposing $\alpha = -\frac{r_c^2}{4\nu t}$, this equation can be rewritten as

$$e^{-\alpha} = 1 - 2\alpha. \tag{3.11}$$

By evaluating α numerically, one obtains the Oseen parameter $\alpha = 1.25643$. Thus, the core size is given by

$$r_c = \sqrt{4\alpha\nu t}. \tag{3.12}$$

Substituting for r_c in equation 3.4, one obtains the simplified form of the Lamb-Oseen equation :

$$u = \frac{\Gamma}{2\pi r}\left(1 - e^{-\alpha\left(\frac{r}{r_c}\right)^2}\right). \tag{3.13}$$

As it can be seen in figure 3.4, the velocity profile now passes through 0 when $r = 0$, thus eliminating the numerical singularity in 2D.

To apply this equation in 3D, the equation is reverse engineered by assuming

$$u = \frac{\Gamma}{4\pi r}\left(\cos\beta_1 - \cos\beta_2\right)\left(1 - e^{-\alpha\left(\frac{r}{r_c}\right)^2}\right). \tag{3.14}$$

By applying the same relations we used to obtain equation 3.7, the Lamb-Oseen Corrected Biot-Savart Law is

$$\vec{u} = \frac{\Gamma}{4\pi}\frac{\vec{r}_1 \times \vec{r}_2}{\|\vec{r}_1 \times \vec{r}_2\|}\vec{r}_0 \cdot \left(\frac{\vec{r}_1}{\|\vec{r}_1\|} - \frac{\vec{r}_2}{\|\vec{r}_2\|}\right)\left(1 - e^{-\alpha\left(\frac{\|\vec{r}_1 \times \vec{r}_2\|}{\|\vec{r}_0\| r_c}\right)^2}\right) \tag{3.15}$$

When evaluating the equation analytically, the Lamb-Oseen profile removes the singularity about $r = 0$. However, when evaluated computationally, equations 3.4 and 3.15 suffers the same numerical singularity as the original Biot-Savart equation. The numerical evaluation of these equations close to the vortex filament would lead to the multiplication of an infinitely

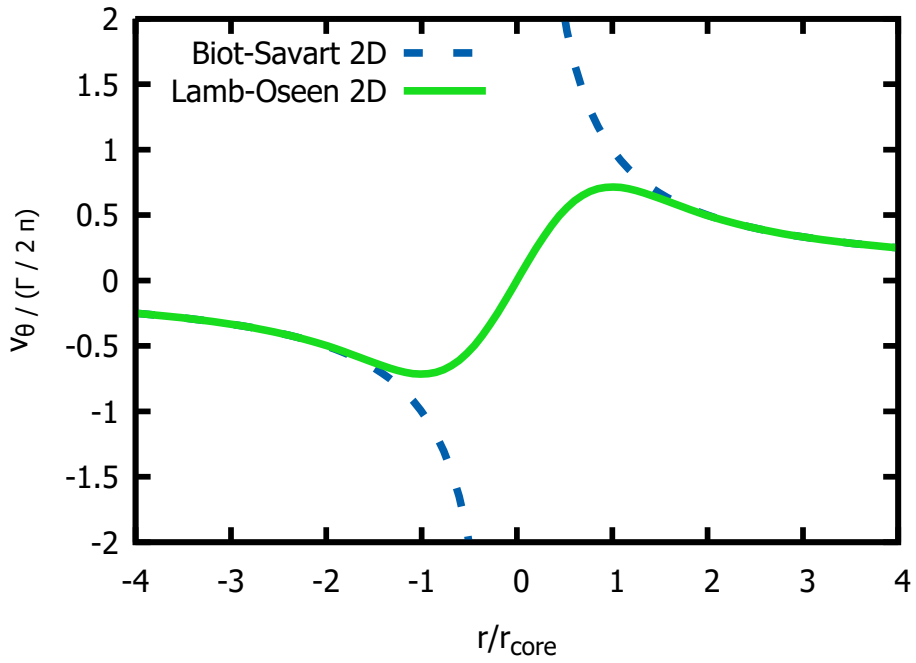

Figure 3.4 The Lamb-Oseen Core Profile

large number by an infinitesimally small number. To remove the numerical singularity in 2D, the Lamb-Oseen equation may be rewritten using a Taylor series:

$$u = \frac{-\Gamma}{2\pi}\left(\cos\beta_1 - \cos\beta_2\right)\sum_{i=1}^{\infty} -\alpha^{2i}\frac{r^{4i-1}}{r_c^{4i} i!} \tag{3.16}$$

The equation for the vortex core size obtained from the Lamb-Oseen equation shows that the core grows with respect to time, as seen in equation 3.12. While this provides a reasonable first assumption to the core growth rate, one must recall that this core size is obtained by solving the Navier-Stokes equation in its laminar form. As such, Squire emitted the hypothesis of adding an eddy (turbulent) viscosity parameter $\delta = 1 + a_1\frac{\Gamma}{\nu}$ to correct the α parameter calculated previously. The value of a_1 is determined empirically. Leishman *et al.* (2002) suggest to keep this parameter relatively small, $\mathcal{O}(10^{-4})$, for best results.

3.1.3 The Vatistas Core Model

The Vatistas Core Model removes the singularity in the Biot-Savart equation by modifying the denominator with a heuristic equation, as shown in the following equation :

$$u = \frac{\Gamma}{2\pi} \frac{r}{\left(r_c^{2n} + r^{2n}\right)^{\frac{1}{n}}}. \tag{3.17}$$

As was done with the Lamb-Oseen Core Model, the Vatistas Core Model can be rewritten in its 3D form :

$$\vec{u} = \frac{\Gamma}{4\pi} \frac{\vec{r}_1 \times \vec{r}_2}{\left(\left\|r_c\vec{r}_0\right\|^{2n} + \left\|\vec{r}_1 \times \vec{r}_2\right\|^{2n}\right)^{\frac{1}{n}}} \vec{r}_0 \cdot \left(\frac{\vec{r}_1}{\left\|\vec{r}_1\right\|} - \frac{\vec{r}_2}{\left\|\vec{r}_2\right\|}\right). \tag{3.18}$$

In this case, the main singularity of the equation is removed as long as r_c is chosen to be greater than 0. The final two sources of a singular solution are obtained when $\vec{P}$ approaches $\vec{r}_1$ or $\vec{r}_2$. This situation is much less likely to occur, therefore a simple cutoff $\vec{u} = \vec{0}$ if $\left\|\vec{P} - \vec{r}_i\right\| < \epsilon$ is applied.

As noted by Dumitrescu and Frunzulica (2004), varying the parameter n will yield different core profiles. As noted in figure 3.5, the Scully Viscous Core Model is obtained when $n = 1$, an approximation to the Lamb-Oseen Core Model is established for $n = 2$, and the Rankine Core Model can be found when $n \to \infty$. Figure 3.6 compares the Vatistas model with $n = 2$ to the Lamb-Oseen core model. These models are very similar to each other.

3.1.4 Vortex Diffusion and Stretching

The strength of a vortex in a fluid fades in time due to viscous diffusion. Equation 3.12 models the core growth through an increase in the vortex core size. As stated in Ananthan *et al.* (2002), Squire (1965) proposed the use of a turbulent eddy viscosity parameter δ to increase the growth rate of the vortex core, as well as the use of an initial core size. Bhagwat and Leishman (2002) then proposed a model to determine the value of the turbulent eddy viscosity:

$$\delta = 1 + a_1 \frac{\Gamma}{\nu}. \tag{3.19}$$

The vortex core size can thus be rewritten as

$$r_c(t) = \sqrt{r_0^2 + 4\alpha \left(1 + a_1 \frac{\Gamma}{\nu}\right) \nu \Delta t}, \tag{3.20}$$

with r_0 being the initial core size.

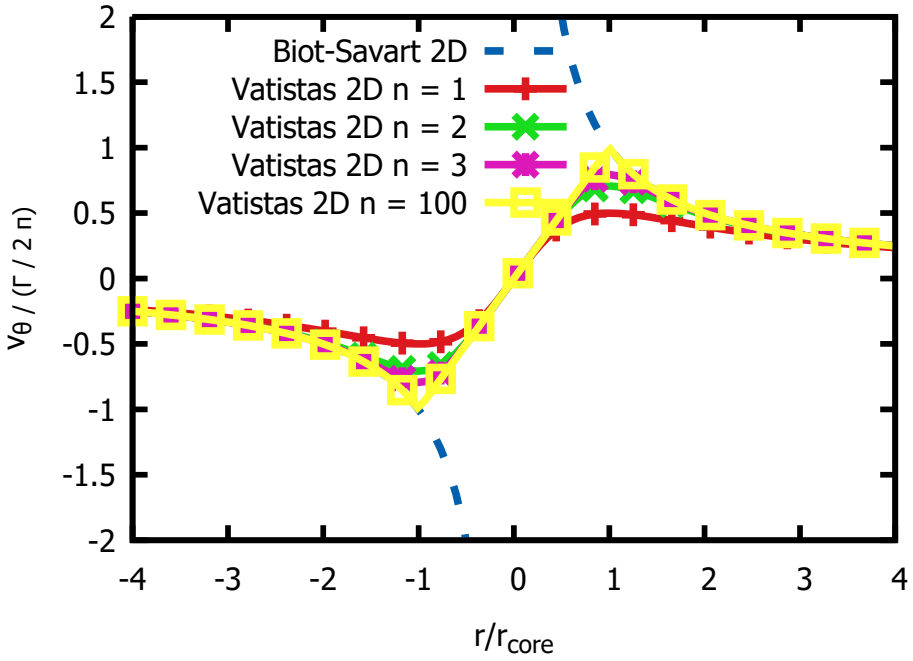

Figure 3.5 The Vatistas Core Model

Ananthan *et al.* (2002) proposes including the effect of strain into this equation as well.

$$r_c = \sqrt{r_0^2 \frac{1}{1+\frac{\Delta l}{l}} + 4\alpha\left(1 + a_1\frac{\Gamma}{\nu}\right)\nu\Delta t} \tag{3.21}$$

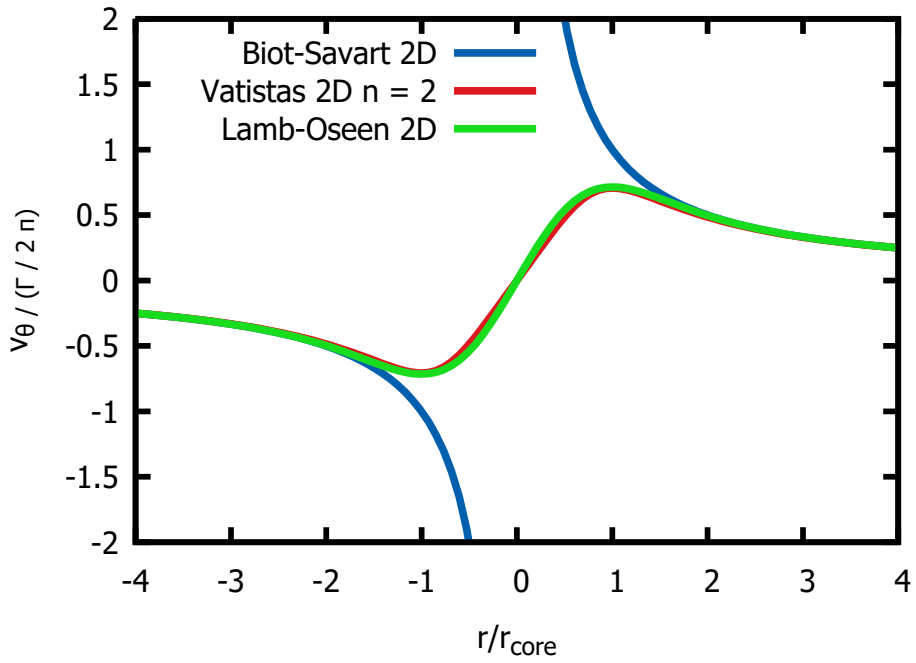

Figure 3.6 Comparison of the Vatistas Core Model

3.2 Ground Effect and Obstacles

One of the primary motivations for this research project was the simulation of helicopter performance near the ground and near obstacles. The problem can be divided in two: the simulation of flow near a flat ground plane and the simulation of flow near arbitrarily shaped objects. As with the modelling of a wing with the vortex-lattice method, the primary goal is to ensure a non-penetrating flow at the obstacle.

When the obstacle is planar and near-infinite, the simplest and most effective method is to place a symmetrical image of the geometry and its wake on the other side of the plane and inverting the sign of the panel strength. The following development proves this.

Consider the effect of an arbitrary SLVE $\vec{r}_0$ on an arbitrary symmetry plane with normal $\vec{n}$ on a point placed on the plane. The symmetric SLVE $\vec{r}_0^{\,s}$ across the plane is defined as follows:

$$\vec{r}_0^{\,s} = \vec{r}_0 - 2\,(\vec{r}_0 \cdot \vec{n})\,\vec{n} \tag{3.22}$$

$$\vec{r}_1^{\,s} = \vec{r}_1 - 2\,(\vec{r}_1 \cdot \vec{n})\,\vec{n} \tag{3.23}$$

$$\vec{r}_2^{\,s} = \vec{r}_2 - 2\,(\vec{r}_2 \cdot \vec{n})\,\vec{n} \tag{3.24}$$

The following operations may be defined:

$$\vec{r}_1^{\,s} \times \vec{r}_2^{\,s} = \vec{r}_1 \times \vec{r}_2 + 2\left[(\vec{n}\cdot\vec{r}_2)\,\vec{r}_1 - (\vec{n}\cdot\vec{r}_1)\,\vec{r}_2\right] \times \vec{n} \tag{3.25}$$

$$\vec{r}_0^{\,s} \cdot \vec{r}_1^{\,s} = \vec{r}_0 \cdot \vec{r}_1 \tag{3.26}$$

$$\vec{r}_0^{\,s} \cdot \vec{r}_2^{\,s} = \vec{r}_0 \cdot \vec{r}_2 \tag{3.27}$$

To respect the non-penetrating flow condition, the following equation must be respected:

$$(\vec{u} + \vec{u}^{\,s}) \cdot \vec{n} = 0. \tag{3.28}$$

Substituting the Biot-Savart equation into the previous equation, one obtains :

$$\begin{aligned}\left[\frac{\Gamma}{2\pi}\frac{\vec{r}_1 \times \vec{r}_2}{\|\vec{r}_1 \times \vec{r}_2\|}\vec{r}_0 \cdot \left(\frac{\vec{r}_1}{\|\vec{r}_1\|} - \frac{\vec{r}_2}{\|\vec{r}_2\|}\right)\right] \cdot \vec{n} \\ + \left[\frac{\Gamma^{\,s}}{2\pi}\frac{\vec{r}_1 \times \vec{r}_2 + 2\left(\left[(\vec{n}\cdot\vec{r}_2)\,\vec{r}_1 - (\vec{n}\cdot\vec{r}_1)\,\vec{r}_2\right] \times \vec{n}\right)}{\|\vec{r}_1 \times \vec{r}_2\|}\vec{r}_0 \cdot \left(\frac{\vec{r}_1}{\|\vec{r}_1\|} - \frac{\vec{r}_2}{\|\vec{r}_2\|}\right)\right] \cdot \vec{n} \\ = 0.\end{aligned} \tag{3.29}$$

Note that

$$2\left(\left[(\vec{n}\cdot\vec{r}_2)\,\vec{r}_1 - (\vec{n}\cdot\vec{r}_1)\,\vec{r}_2\right] \times \vec{n}\right) \cdot \vec{n} = 0 \tag{3.30}$$

due to the properties of the mixed product. As such, equation 3.28 is true if and only if

$$\Gamma^{\,s} = -\Gamma. \tag{3.31}$$

Therefore, to model the ground plane with a symmetry plane, all SLVEs must be mirrored and their circulation inverted to respect the non-penetrating flow condition. To save memory, these symmetrical panels need not be modelled. Their influence is simply calculated at runtime using the original SLVEs geometric definition.

To model the flow around an arbitrarily shaped object, the object's surface is modelled with vortex panels. However, when vortex panels form a closed surface, the linear system of equations generated becomes singular. Solving this system leads to numerical divergence. As explained by Srivastava and Mook (1994), "if the no-penetration condition is satisfied on $N-1$ panels then the remaining panel is automatically impermeable [due to the continuity requirement]". The N^{th} equation is therefore overdetermined, rendering the influence matrix A singular. To remedy this issue, two approaches were attempted. The first approach is to simply eliminate an equation from the system created by the closed body (Srivastava and Mook, 1994). The second approach is to modify the equation of one panel on the closed body

to

$$\sum_{i}^{N_{Body}} \Gamma_i = 0, \tag{3.32}$$

thus closing the system of equations.

While the presented methods for the ground effect framework work well for steady calculations, their use in unsteady simulations can be limited. The use of a discrete timestep, if taken too large, may allow a wake element to flow through the symmetry plane or the closed surface. To keep this from happening, one would need to verify the position of each wake element with respect to the symmetry plane and the closed body.

While being a simple method to implement, it should be noted that the rollup procedure increases in complexity with every timestep as new panels are added into the simulation. To limit the computational cost, it is possible to remove the oldest panels of a simulation. To conserve the total circulation (Kelvin's theorem), their circulation must be added to their adjacent panels. In fixed wing applications, this can be done with minimal error, as the aircraft distances itself from the cutoff point at a rapid rate. In rotary wing applications, however, the rotorcraft tends to remain close enough to its wake that the cutoff may have a considerable impact on the solution.

Additionally, panels subjected to strong shearing velocities may be deformed unrealistically, inducing numerical error. Figure 3.7 shows an example of such deformation. Consider the SLVE depicted at time t_0. The presence of the ground plane tends to push the outboard point of the SLVE further out, while the inboard points tend to remain below the rotor disk. A certain amount of recirculation in the inboard portion below the rotor disk also pushes the inboard control point of the SLVE. After a few iterations, the inboard control point may also be ejected through the rotor disk. These deformations may create convergence issues, as the SLVE passes directly through the rotor plane.

3.2.1 Vortex Particle Free-Wake Model

In this free-wake mode, as presented by Winckelmans and Leonard (1993), the wake is represented as vortex particles (vortons). Each vorton can be represented by a position vector, $\vec{x}$ and a circulation vector, $\vec{\alpha}$. Similar to the CVC wake model, a buffer of panels is initially shed from the lifting surface. It is subsequently replaced by vortex particles (Willis *et al.*, 2007), as can be seen in figure 3.8.

The circulation vector is defined as

$$\vec{\alpha} = \vec{\omega} vol, \tag{3.33}$$

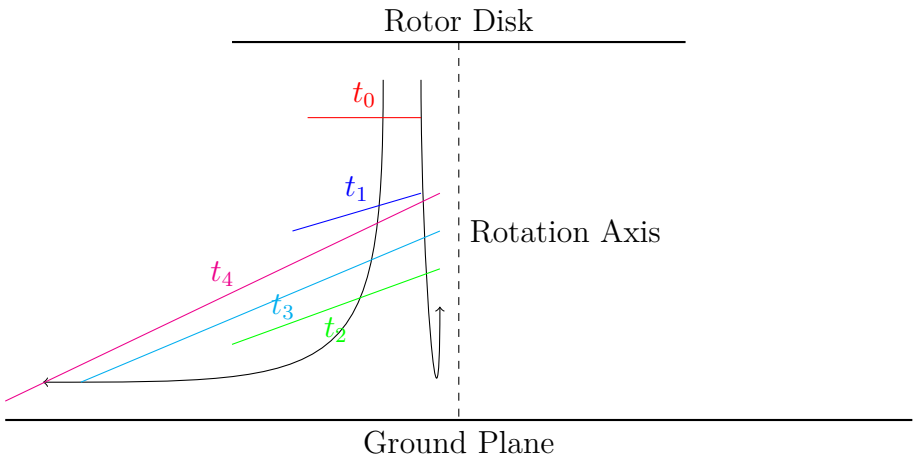

Figure 3.7 Unrealistic Deformation in Ground Effect

where *vol* is the volume of the vorticity tube represented by the vorton. The circulation of an SLVE is given by $\Gamma = \omega\pi r^2$, with r as the vorticity tube's radius (core size). The right-hand side of equation 3.33 may be rewritten as follows :

$$\vec{\omega} vol = \left(\omega \frac{\vec{r}_0}{\|\vec{r}_0\|}\right)\left(\pi r^2 \|\vec{r}_0\|\right) = \Gamma \vec{r}_0. \tag{3.34}$$

Simply put, the vorticity of a vortex particle replacing an SLVE is given by

$$\vec{\alpha} = \Gamma \vec{r}_0. \tag{3.35}$$

Winckelmans and Leonard (1993) present an adapted Algebraic Smoothing viscous core model. The velocity of a vorton i on a point $\vec{P}$, using the Algebraic Smoothing core model, is given by

$$\vec{u}_{i,\vec{P}} = -\frac{\left\|\vec{P} - \vec{x}\right\|^2 + \frac{5}{2} r_c^2}{4\pi\left(\left\|\vec{P} - \vec{x}\right\|^2 + r_c^2\right)^{\frac{5}{2}}}\left(\vec{P} - \vec{x}\right) \times \vec{\alpha}. \tag{3.36}$$

In the previous models, the deformation (strain) of a vortex filament was implicitly calculated through the displacement of the SLVE's endpoints. This also intrinsically respects the no-divergence law in the fluid. To respect this law for a vorton, its strain must be calculated differently. The representation of a vorton as a single point requires the strain to be calculated explicitly, based upon the local velocity gradient $\nabla\vec{u}$ at the vorton's position. Considering that the local velocity is the sum of the velocity contributions of all other vortex elements,

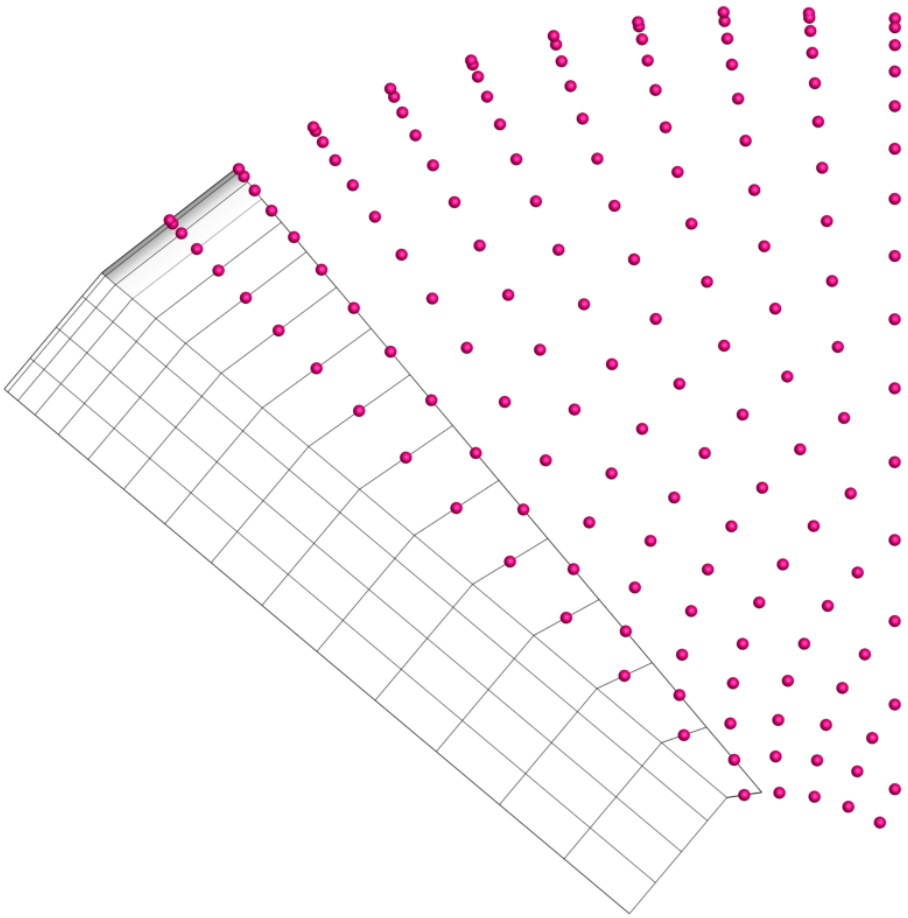

Figure 3.8 Replacing Panels with Vortex Particles

the strain may also be calculated on a point-to-point basis. The strain of a vorton at point $\vec{P}$ is classically given by

$$\frac{d\vec{\alpha}_{\vec{P}}}{dt} = \left(\vec{\alpha}_{\vec{P}} \cdot \nabla\right) \vec{u}_{\vec{P}}. \tag{3.37}$$

The vorton with algebraic smoothing proposed by Winckelmans and Leonard (1993) produces

the following strain, if viscosity is neglected:

$$\frac{d\vec{\alpha}_{\vec{P}}}{dt} = \frac{1}{4\pi}\left[-\frac{\left\|\vec{P}-\vec{x}\right\|^2+\frac{5}{2}r_c^2}{\left(\left\|\vec{P}-\vec{x}\right\|^2+r_c^2\right)^{\frac{5}{2}}}\vec{\alpha}_{\vec{P}}\times\vec{\alpha}_{\vec{x}}+ 3\frac{\left\|\vec{P}-\vec{x}\right\|^2+\frac{7}{2}r_c^2}{\left(\left\|\vec{P}-\vec{x}\right\|^2+r_c^2\right)^{\frac{7}{2}}}\left(\vec{\alpha}_{\vec{P}}\cdot\left(\vec{P}-\vec{x}\right)\right)\left(\left(\vec{P}-\vec{x}\right)\times\vec{\alpha}_{\vec{x}}\right)\right]. \quad (3.38)$$

The vortex panels of the lifting surface and the wake buffer also create strain on the vortons. To simplify the strain calculation, the vortex filaments composing these vortex panels are treated as vortons. Note that vorton strain is the equivalent of vortex stretching for vortex filaments. The same principles of vortex diffusion may apply to vortex particles.

3.3 Summary

The implementations made to the classic UVLM were discussed in this chapter. The reason for the numerical instability of the Biot-Savart law was explained. The Lamb-Oseen and Vatistas core models were implemented in an effort to remove this numerical instability. It was shown that the Vatistas core model could also be used as an approximation to many other core models, Lamb-Oseen's included. The numerical problems caused by ground effect were also presented. The vorton wake was implemented in order to remove these issues.

CHAPTER 4 VALIDATING THE UVLM

This chapter will present the validation of the developments presented in chapter 3. The code being tested was programmed using an object-oriented approach in C++. The code inherits from an initial UVLM framework for fixed-wing aircraft, similar to that described by Chrust *et al.* (2015). It is capable of running on multiple processors using simple OpenMP pragma instructions. The code is compiled as a library that is accessible through a Python interface. This interface allows the user to set up test cases with relative ease, without needing to recompile the VLM code.

Three test cases were selected to validate the code :

- the Caradonna-Tung rotor in hover (Caradonna and Tung, 1981),
- the Caradonna rotor in climb (Caradonna, 1999),
- the Lynx tail rotor in ground effect (Light, 1993).

These cases were selected for having the following characteristics :

- purely axial flight;
- thrust coefficient data available;
- tip-vortex position data available.

4.1 Caradonna-Tung Rotor in Hover

The Caradonna-Tung rotor is a two-bladed rotor with an untwisted NACA0012 blade profile. The rotor radius is 1.143 m and has an aspect ratio of 6. This test case was used to evaluate the choice of vortex core model and vortex core size. The geometric model was also used as a baseline for testing the wake model implementation. Table 4.1 shows the selected data from the test case and summarizes the above information.

4.1.1 Thrust Convergence

In order to evaluate the effect of the viscous core model and the viscous core size, a sweep of viscous core size was completed for each core model. For a vortex panel wake, the core size

Table 4.1 Conditions for the Caradonna-Tung Rotor in Hover

Test ID	1	2	3
Airfoil	NACA0012		
Rotor Radius (m)	1.143		
Root Cutout Radius (m)	0.1905		
Blade Chord (m)	0.1905		
Blade Twist (°)	0		
Number of Blades	2		
Rotor Solidity σ	0.1061		
Collective Pitch (°)	5	8	12
Rotor Speed (RPM)	1250	1250	1800
C_T	0.0021	0.0046	0.0079

is determined using the initial distance between adjacent viscous filaments. In other words, the core size input by the user r_c^* is equivalent to

$$r_c^* = \frac{r_c}{l_0}, \tag{4.1}$$

where l_0 is the length of the longest vortex filament in the vortex panel. In the case of vortex particles, the core size is inherited from the filament from which it was issued. The core size r_c^* was varied from 0.1 to 0.5, with intervals of 0.1. Tables 4.2, 4.3 and 4.4 show the thrust coefficients obtained when evaluating the core models and core sizes. The tests were run for 10 rotor revolutions, with 10° increments in the rotor's position at each iteration, i.e. the tests were run for 360 iterations. Note that the Lamb-Oseen, Scully and Vatistas core models were used with a vortex panel free-wake, while the Algebraic Smoothing model was used with a vortex particle free-wake. The thrust coefficient is averaged over the last 2 rotor revolutions, with the uncertainty representing the standard deviation over the same period. This is done to reduce the influence of the unconverged wake on the results.

In general, increasing the core size tends to reduce the amount of thrust generated by the simulated rotor. The increased core size tends to reduce movement in the wake. The wake remains closer to the rotor hub, increasing the blade downwash. This decreases the efficiency of the rotor and thus decreases the thrust generated by the rotor. The standard deviation calculated in the converged wake remains within the same order of magnitude across all core models and core sizes.

The Lamb-Oseen and Algebraic Smoothing core models, however, seem to remain relatively insensitive to the core size once the flow is in a converged state. In the case of the vortex

Table 4.2 Effect of Core Model and Core Size on Thrust Coefficient for $\theta = 5.0°$

	Core Model			
Core Size	Lamb Oseen	Scully	Vatistas $n = 2$	Algebraic Smoothing
[-]	$C_T * 10^4$ [-]			
0.1	22.93 ± 1.44	23.44 ± 4.39	22.12 ± 1.266	21.48 ± 0.38
0.2	24.02 ± 1.55	22.16 ± 7.29	22.58 ± 0.223	21.48 ± 0.25
0.3	23.62 ± 0.92	21.75 ± 7.73	21.04 ± 0.146	21.28 ± 0.41
0.4	23.72 ± 1.79	18.79 ± 5.70	20.32 ± 0.235	21.40 ± 0.40
0.5	23.73 ± 1.09	17.40 ± 3.98	19.27 ± 0.481	21.36 ± 0.44
[-]	Error from Experimental Data [%]			
0.1	9.2 ± 6.9	11.6 ± 20.9	5.3 ± 60.3	2.3 ± 1.8
0.2	14.4 ± 7.4	5.5 ± 34.7	7.5 ± 10.6	2.3 ± 1.2
0.3	12.5 ± 4.4	3.8 ± 36.8	0.2 ± 6.9	1.3 ± 2.0
0.4	13.0 ± 8.5	-10.5 ± 27.1	-3.2 ± 11.2	1.9 ± 1.9
0.5	13.0 ± 5.2	-17.1 ± 19.0	8.2 ± 22.9	1.7 ± 2.1

Table 4.3 Effect of Core Model and Core Size on Thrust Coefficient for $\theta = 8.0°$

	Core Model			
Core Size	Lamb Oseen	Scully	Vatistas $n = 2$	Algebraic Smoothing
[-]	$C_T * 10^4$ [-]			
0.1	46.93 ± 1.45	44.99 ± 1.65	46.37 ± 2.97	43.04 ± 0.53
0.2	46.52 ± 1.60	43.92 ± 0.45	45.26 ± 0.52	43.03 ± 0.52
0.3	46.36 ± 1.02	43.15 ± 0.77	42.95 ± 1.36	43.01 ± 0.54
0.4	46.17 ± 1.18	40.79 ± 1.05	42.41 ± 0.52	43.09 ± 0.51
0.5	46.01 ± 0.88	39.83 ± 1.78	42.11 ± 1.04	42.53 ± 0.64
[-]	Error from Experimental Data [%]			
0.1	2.0 ± 3.2	-2.2 ± 3.6	0.8 ± 6.5	-6.4 ± 1.2
0.2	1.1 ± 3.5	-4.5 ± 1.0	-1.6 ± 0.9	-6.5 ± 1.1
0.3	0.8 ± 2.2	-6.2 ± 1.7	-6.6 ± 3.0	-6.5 ± 1.2
0.4	0.4 ± 2.6	-11.3 ± 2.3	-7.8 ± 1.1	-6.3 ± 1.1
0.5	0.0 ± 1.9	-13.4 ± 3.9	-8.5 ± 2.3	-7.5 ± 1.4

particle wake, this may be explained by a greater distance between the vortex particles. The control points in a panel method are connected to each other using vortex filaments and therefore remain relatively close together, whereas vortex particles are completely free from one another. However, in the case of the Lamb-Oseen core model, the reason behind the insensitivity is admittedly unknown to the author.

Figures 4.1, 4.2, 4.3 and 4.4 show the evolution of the thrust coefficient with each solver

Table 4.4 Effect of Core Model and Core Size on Thrust Coefficient for $\theta = 12.0°$

	Core Model			
Core Size	Lamb Oseen	Scully	Vatistas $n = 2$	Algebraic Smoothing
[-]	$C_T * 10^4$ [-]			
0.1	81.67 ± 1.71	77.90 ± 1.01	82.24 ± 0.42	75.64 ± 1.21
0.2	82.94 ± 1.05	72.75 ± 1.98	78.15 ± 1.16	75.73 ± 1.19
0.3	82.47 ± 1.44	69.19 ± 2.17	78.22 ± 16.31	75.77 ± 1.16
0.4	82.69 ± 1.49	70.43 ± 0.49	67.49 ± 3.78	75.79 ± 1.14
0.5	82.43 ± 1.60	66.68 ± 1.14	70.16 ± 1.49	75.80 ± 1.11
[-]	Error from Experimental Data [%]			
0.1	3.4 ± 2.2	-1.4 ± 1.3	4.1 ± 0.5	-4.3 ± 1.5
0.2	5.0 ± 1.3	-7.9 ± 2.5	-1.1 ± 1.5	-4.1 ± 1.5
0.3	4.4 ± 1.8	-12.4 ± 2.7	-1.0 ± 20.6	-4.1 ± 1.5
0.4	4.7 ± 1.9	-10.8 ± 0.6	-14.6 ± 4.8	-4.1 ± 1.4
0.5	4.3 ± 2.0	-15.6 ± 1.4	-11.2 ± 1.9	-4.1 ± 1.4

iteration. These graphs show similarities in the way the thrust is developed. During the first iteration, a large amount of thrust is produced. This is due to the impulse start of the rotor, where the rotor rotation speed jumps from 0 to the desired velocity within 1 iteration. This generates a large amount of lift, as expected from the unsteady Bernouilli equation (Katz and Plotkin, 2001). The lift then decreases rapidly in the next iteration, as the wake generated from this impulse start generates a strong downwash on the blade. As the blade moves away from its own initial wake and towards the other blade's wake, the thrust begins to rise again. This is caused by the initial wake of the opposing blade that generates and upwash, increasing the lift generated by the blade. Once the blade passes above the opposing blade's initial wake, the thrust starts to decrease and the wake starts moving downward at a faster rate, starting to grow. From this point on, there will always be wake elements beneath the blade. As the wake grows, the thrust produced by the blade diminishes, as the cumulative downwash from the wake grows as well. Once the wake development reaches a steady state, the thrust developed by the blade will oscillate around a fixed value.

As can be seen in figures 4.1, 4.2 and 4.3, the vortex panel wake method tends to converge after approximately 5 rotor revolutions. However, there tends to be a large amount of noise in the thrust generated by the rotor. The Scully and Vatistas core models seem to be prone to large excursions in thrust generation that may be explained by the passing of a strong vortex filament near the rotor blade. While core models smooth the Biot-Savart equations, using a core size that is too small may still lead to numerical instabilities. This may be indicative of an issue in the current methodology, where the core size is a ratio of the longest

filament in a vortex panel upon its release from the blade's trailing edge.

The vorton wake model, however, seems to be free of such variations once the wake development reaches its steady state (figure 4.4). The use of a point vortex tends to increase the relative distance between the wake elements and the blade elements, thus resulting in a smooth and filtered thrust generation. The thrust reaches a steady oscillation every half rotor rotation (or, in the generalized case, every $\frac{1}{N}$ revolutions). This may be explained by the continued presence of the initial impulse wake and the effect of tip rollup.

4.1.2 Tip Vortex Position

Figures 4.5, 4.6, 4.7 and 4.8 show the position of the tip vortex in time (represented as the wake age). The solid lines represent the averaged position over the two final rotations of the simulation, while the dotted lines represent the standard deviation. As predicted by momentum theory, the experimental data show the tip vortex contracts radially below the rotor. Furthermore, the tip vortex visibly accelerates in the axial direction once the opposing blade passes overhead (at 180° in this case). This general trend is visible across all wake and core models. The Lamb-Oseen and Algebraic Smoothing core models are visibly less sensitive to the choice of core size. Furthermore, the wake converges to steady positions. The Scully and Vatistas core models show stronger variations in the tip vortex position. This may be indicative that the Scully and Vatistas core models failed to converge to a final solution in the imposed 10 revolutions, as can be corroborated by figures 4.2 and 4.3. The Scully and Vatistas core models may require further iterations to converge fully or a more stable numerical integration scheme.

4.1.3 Required Power

Of the stated viscous core models and wake models, the Vortex Particle wake with algebraic smoothing was selected for further study. The rapid convergence of the thrust parameter, the stability of the wake position and the model's insensitivity to core size makes the model an interesting platform for testing. The UVLM calculates the induced drag on a lifting surface. The drag calculation, however, tends to require more time to converge, as this parameter is sensitive to small variations in lift. The convergence characteristics of the vorton wake permit the calculation of the power coefficient of the rotor within the allotted number of iterations. Using momentum theory to determine the ideal power, it is possible to calculate the Figure of Merit of the rotor in the simulation. Tables 4.5, 4.6, 4.7 summarize the results. While Caradonna and Tung (1981) did not present the power required for their test rig, the obtained values are typical of rotor blades unoptimized for hovering flight. Considering that

the Caradonna-Tung rotor has a low aspect ratio, relatively high disk loading and no twist, it can be assumed the rotor is unoptimized. A further consideration is that the current state of the UVLM model does not take into account viscous forces. The Figure of Merit would be lowered if these effects are added.

Table 4.5 Vortex Particle Wake Power Calculation ($\theta = 5.0$)

Core Size	$C_T * 10^4$	$C_P * 10^4$	FM
0.1	21.48 ± 0.038	1.04 ± 0.01	0.673381 ± 0.010964
0.2	21.48 ± 0.025	1.04 ± 0.01	0.673704 ± 0.007411
0.3	21.28 ± 0.041	1.04 ± 0.01	0.668943 ± 0.012414
0.4	21.40 ± 0.040	1.04 ± 0.01	0.672654 ± 0.011550
0.5	21.36 ± 0.044	1.04 ± 0.01	0.672570 ± 0.012816

Table 4.6 Vortex Particle Wake Power Calculation ($\theta = 8.0$)

Core Size	$C_T * 10^4$	$C_P * 10^4$	FM
0.1	43.04 ± 0.53	3.01 ± 0.01	0.663366 ± 0.009272
0.2	43.03 ± 0.52	3.01 ± 0.01	0.663313 ± 0.009243
0.3	43.01 ± 0.54	3.01 ± 0.01	0.663050 ± 0.009537
0.4	43.09 ± 0.51	3.01 ± 0.01	0.664171 ± 0.009013
0.5	42.53 ± 0.64	2.99 ± 0.02	0.656038 ± 0.011446

Table 4.7 Vortex Particle Wake Power Calculation ($\theta = 12.0$)

Core Size	$C_T * 10^4$	$C_P * 10^4$	FM
0.1	75.64 ± 1.21	6.74 ± 0.07	0.689756 ± 0.017190
0.2	75.73 ± 1.19	6.75 ± 0.07	0.690782 ± 0.016964
0.3	75.77 ± 1.16	6.75 ± 0.06	0.691038 ± 0.016682
0.4	75.79 ± 1.14	6.75 ± 0.06	0.690971 ± 0.016377
0.5	75.80 ± 1.11	6.76 ± 0.06	0.690765 ± 0.016023

The simulation was run on Calcul Québec's Mp2 server, hosted by the Sherbrooke University. Twelve cores were used for each calculation. The core model execution times are compared in figure 4.9. The Vorton wake is shown to take considerably more time than the panel wakes. This is due to the evaluation of the strain on each vortex particle. The calculation time for the core models used by panel wakes are shown to be similar. Quadratic increase in calculation time is noted for all wake and core models, as expected.

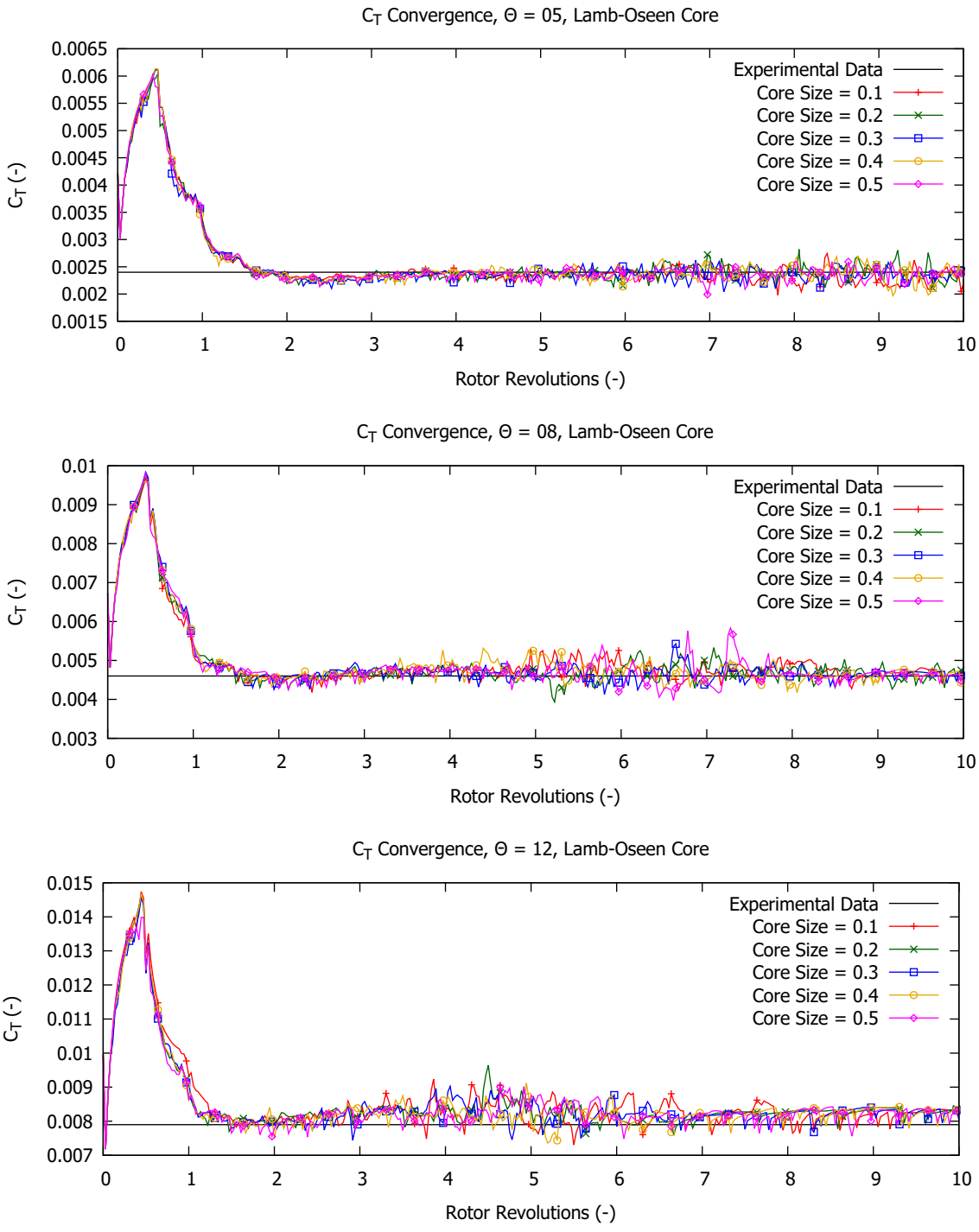

Figure 4.1 Lamb-Oseen Core Model Convergence Graphs

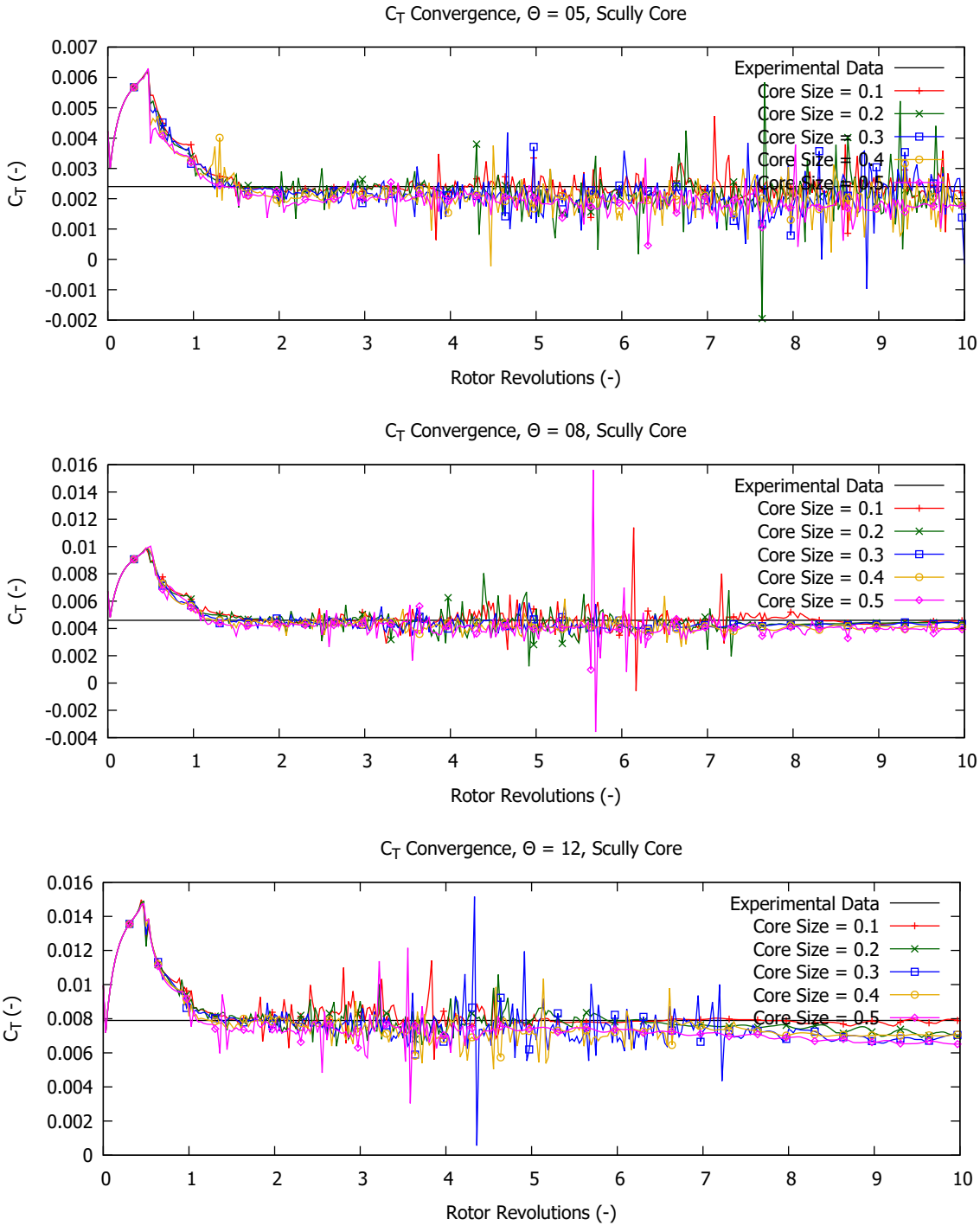

Figure 4.2 Scully Core Model Convergence Graphs

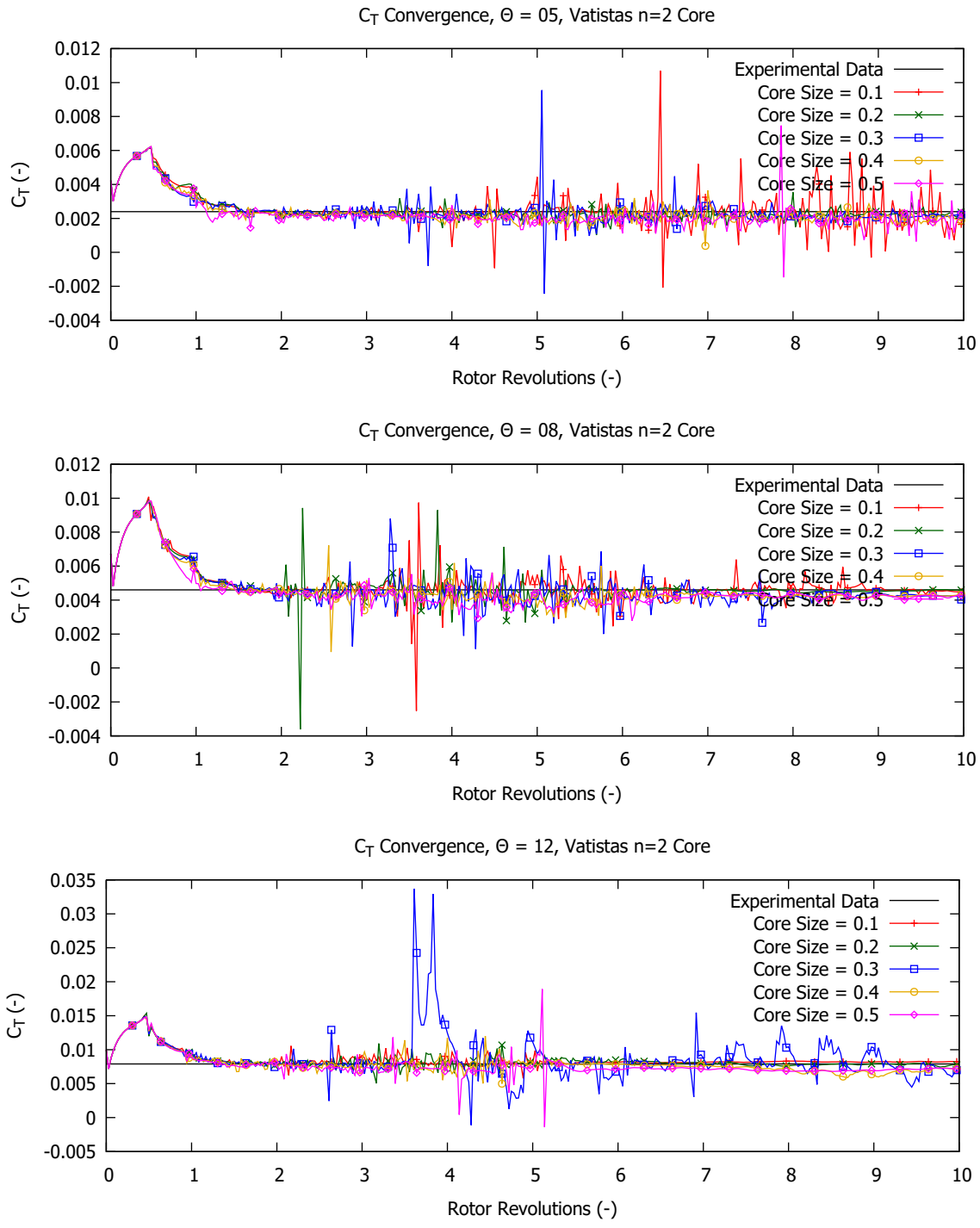

Figure 4.3 Vatistas $n = 2$ Convergence Graphs

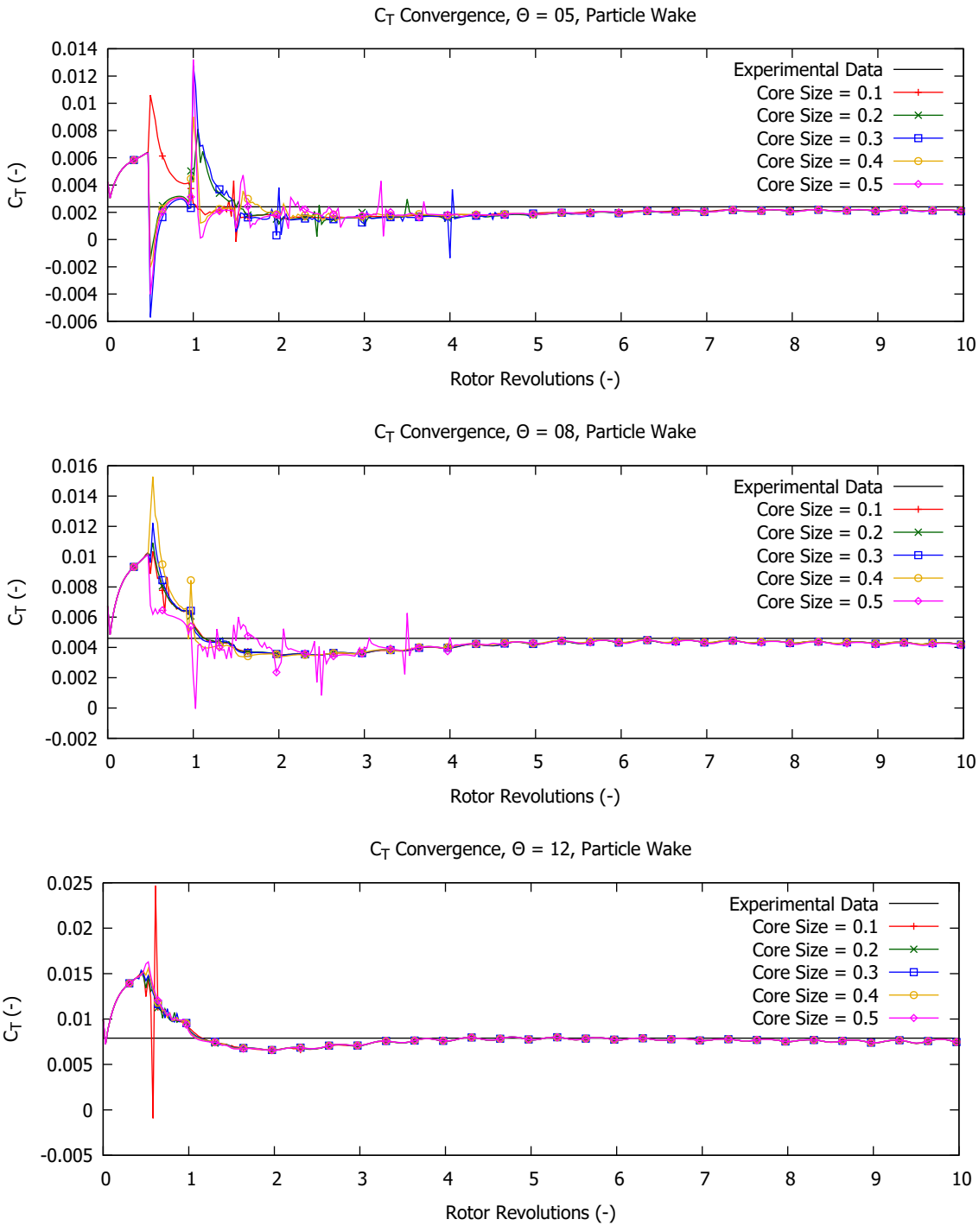

Figure 4.4 Vortons with Algebraic Smoothing Convergence Graphs

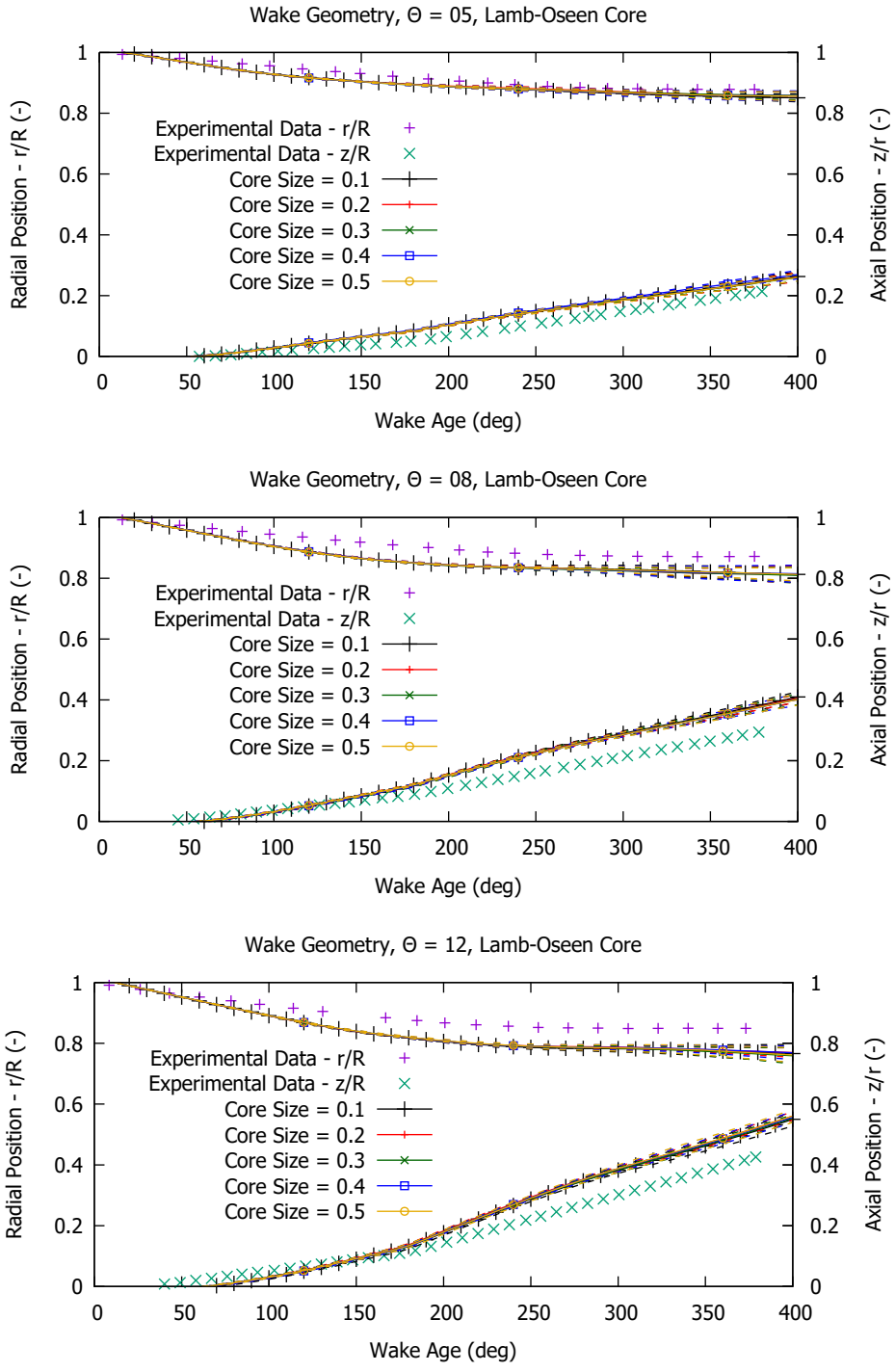

Figure 4.5 Wake Geometry - Lamb Oseen Core Model

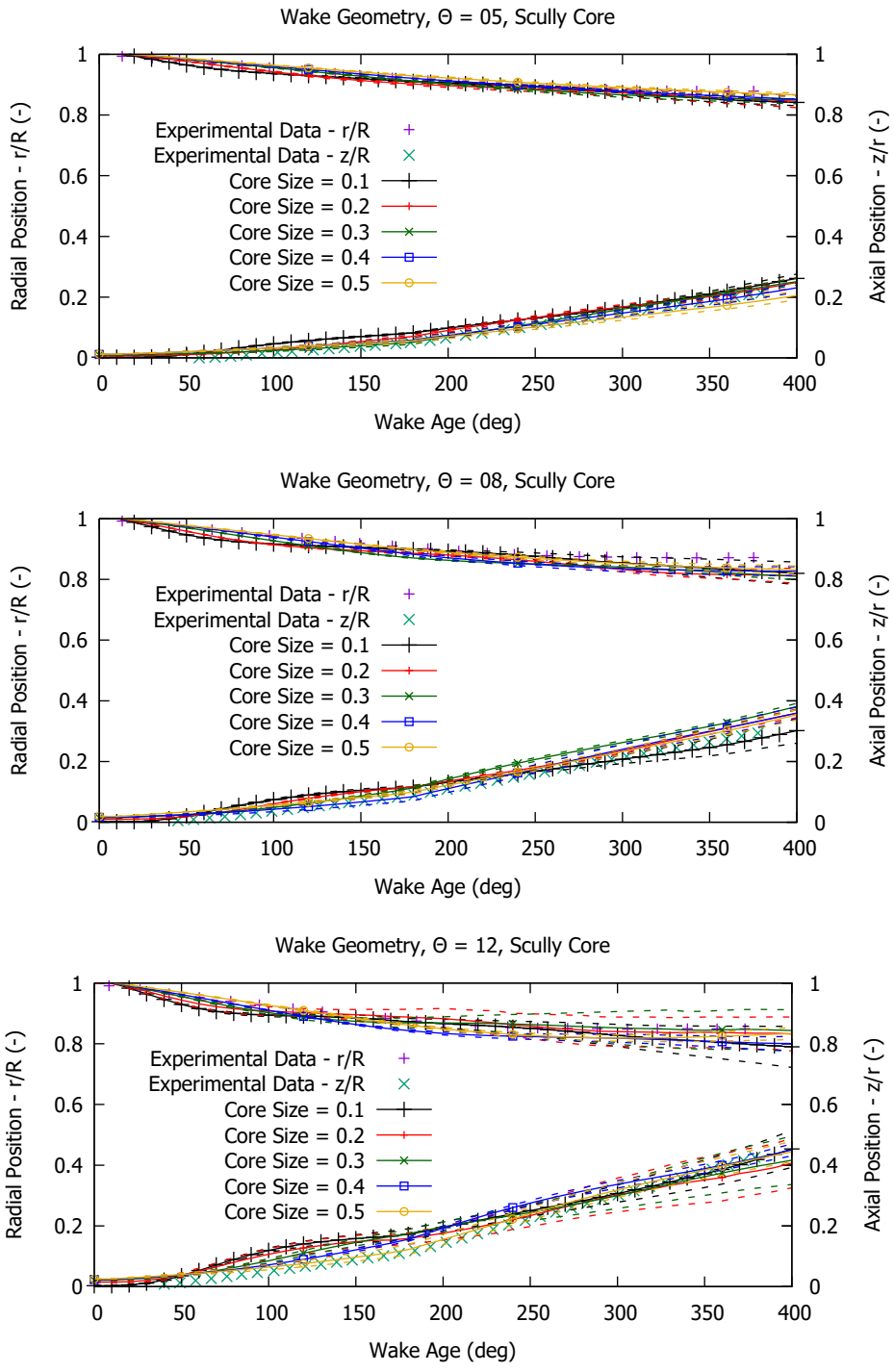

Figure 4.6 Wake Geometry - Scully Core Model

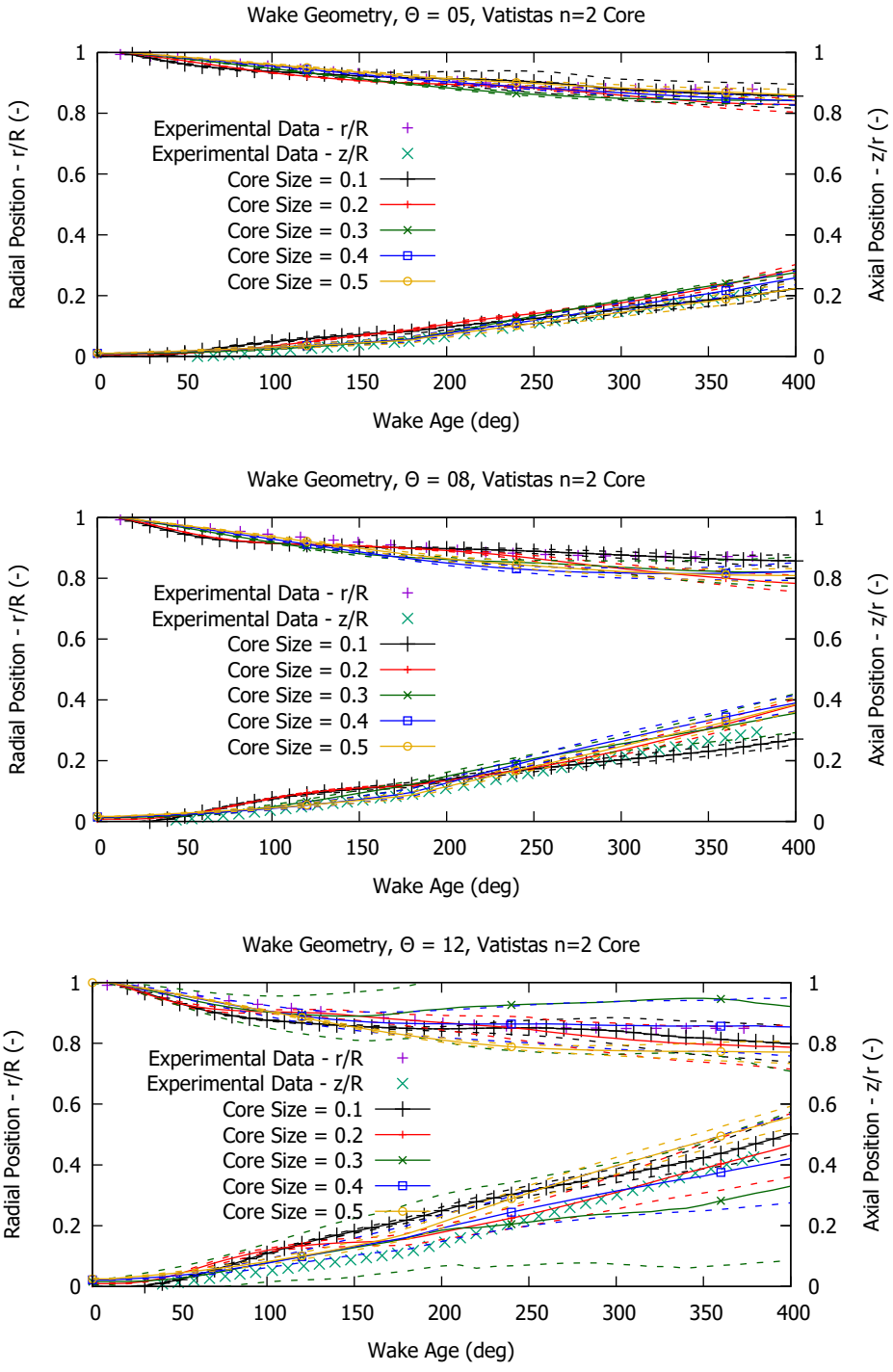

Figure 4.7 Wake Geometry - Vatistas $n = 2$ Core Model

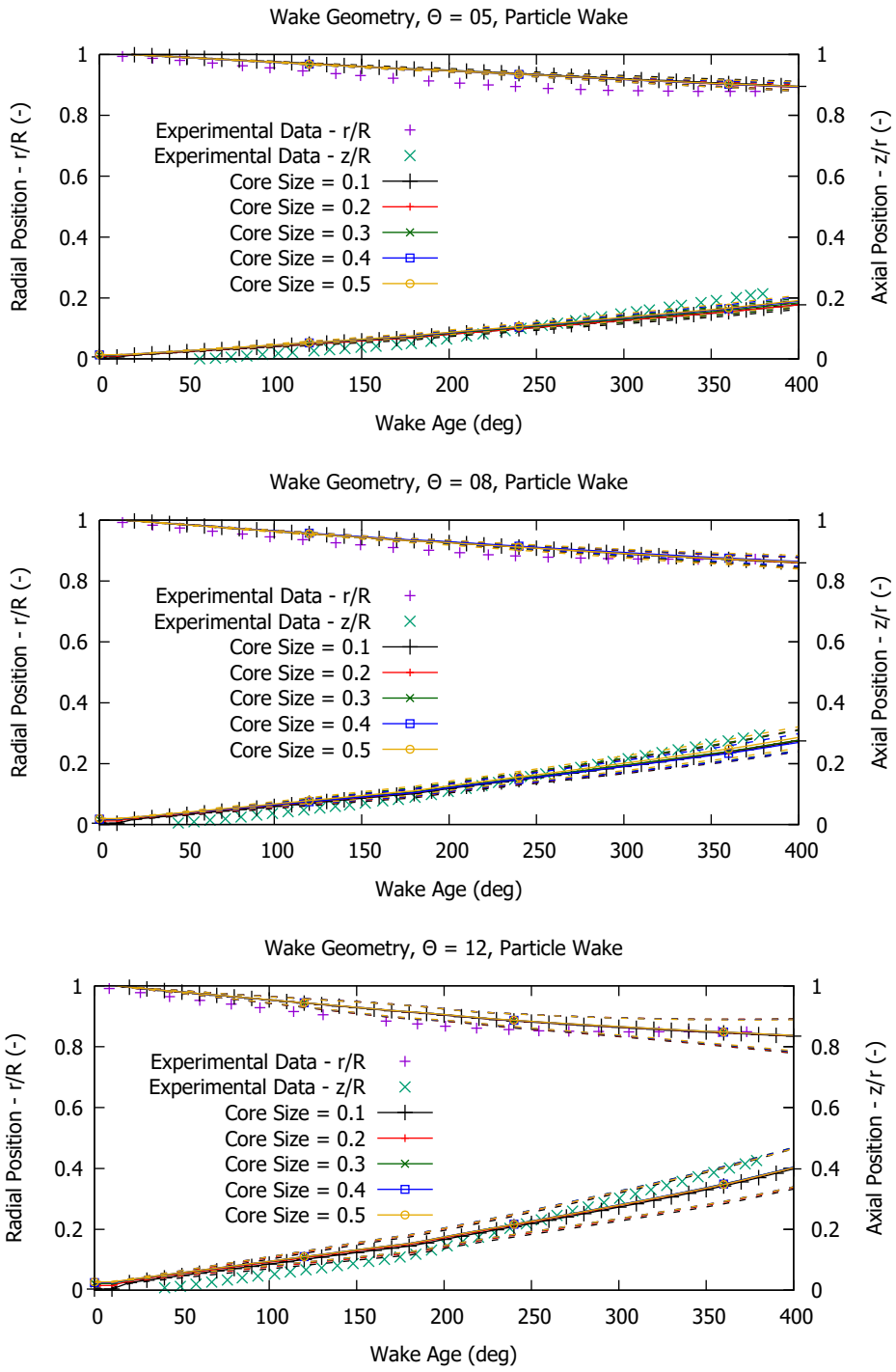

Figure 4.8 Wake Geometry - Vorton with Algebraic Smoothing Core Model

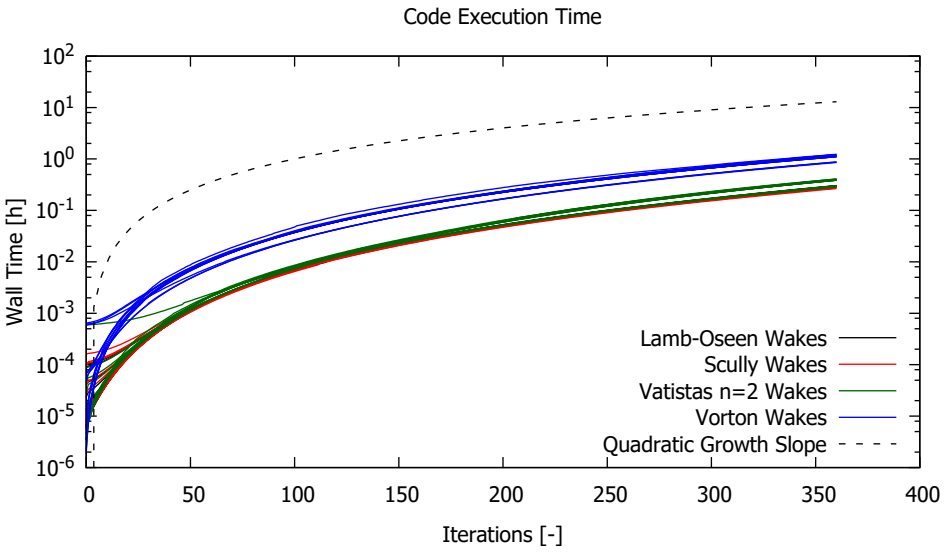

Figure 4.9 Comparison of Core Model Execution Time

4.2 Caradonna Rotor in Climb

The Caradonna rotor is a two-bladed rotor with an untwisted, symmetric Bell profile airfoil. The rotor radius is 1.0414m and the chord is 0.0762m, leading to an aspect ratio of 13.67. In this report, the test case is used to validate the tip vortex positioning and torque calculations of the UVLM. Note that the vortex particle wake model was used for these calculations, with a core size of $r_c^* = 0.4$. The timestep was selected for the rotor to advance 10° at each iteration and the backward Euler timestepping scheme was used. Table 4.8 summarizes the test case. The case is split into two sweeps, the first being a collective angle sweep for a constant climb rate, the second being a climb rate sweep for constant collective angle. The simulations were run for 20 rotor rotations. All presented results were averaged over the final two rotations.

Table 4.8 Conditions for the Caradonna Rotor in Axial Flight

Test ID	1	2	3	4	5	6	7	8	9	10	11	12
Airfoil	Bell Profile											
Rotor Radius	1.0414m											
Root Cutout	0.0762m											
Blade Chord	0.0762m											
Blade Twist	0°											
Number of Blades	2											
Rotor Speed	1800 RPM											
Collective Pitch	6°	8°	9°	10°	11°	12°	11°					
Climb Inflow Ratio * 10^4	54						0	100	110	150	200	400

4.2.1 Thrust in Climb

Figure 4.10 shows the variation of the thrust coefficient with increasing rate of climb. There is a clear tendency for the rotor thrust to vary linearly with the climb rate. This tendency was predicted with blade element theory. The increased inflow in the rotor caused by the climb rate decreases the effective angle of attack of the blade, thus decreasing the generated thrust.

4.2.2 Figure of Merit Variation

The Figure of Merit obtained through simulation may be compared to the results found in Caradonna (1999). Figure 4.11 shows the variation of the Figure of Merit with climb rate.

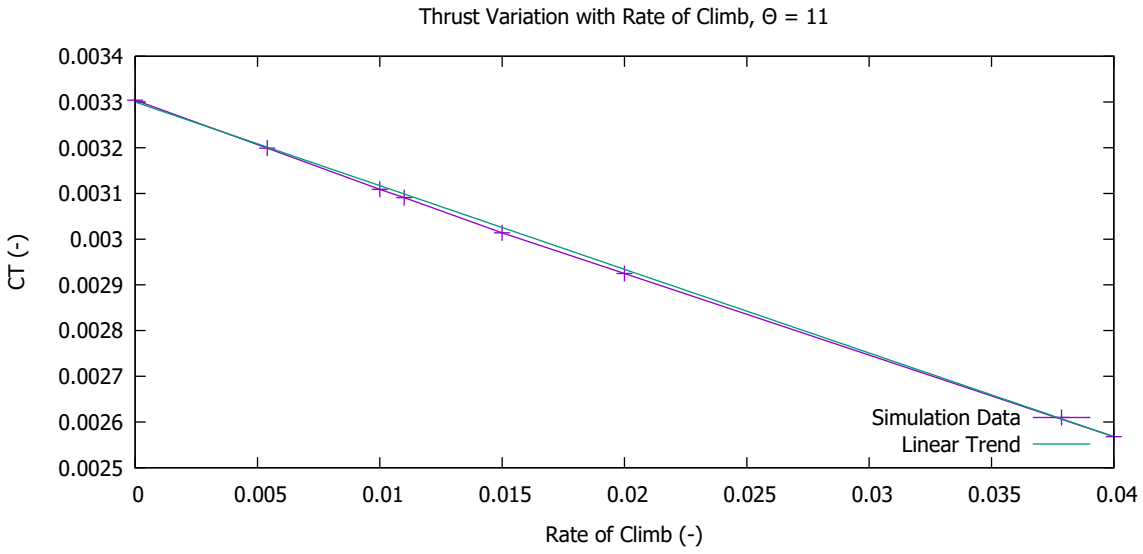

Figure 4.10 Variation of Thrust with Climb Rate

Once again, there is a distinct linear tendency in the variation of the figure of merit in both the experimental and simulation data. As explained by Caradonna (1999), the drop in Figure of Merit in the experimental data may be caused by experimental error, possibly due to rotor imbalance and thermal drift. Caradonna also explains that the expected variation of the Figure of Merit would be a continued linear tendency up to the hover phase, as presented in the UVLM results. The Figure of Merit is also noted to be higher in the simulation data when compared to the experimental results. This may be caused by the inviscid nature of the UVLM, which only calculates the induced drag on the lifting surface. Viscous coupling algorithms, as presented in Gallay and Laurendeau (2015) and Parenteau *et al.* (2018) would permit this calculation and would merit further investigation.

Figure 4.12, presenting the Figure of Merit for a constant rate of climb, corroborates this requirement. The Figure of Merit is shown to vary linearly with collective angle. However, it is largely overestimated. Consider the following equation :

$$FM = \frac{C_{P_{Ideal}}}{C_{P_{Real}}} = \frac{C_{P_{Ideal}}}{\kappa C_{P_{Ideal}} + C_{P_{Viscous}}}. \tag{4.2}$$

The viscous term of the right-hand side of the equation is not supported by the UVLM implementation at the time of this writing. The κ factor represents an empirical factor that takes into account various physical effects. The UVLM calculates a portion of this factor. Recalling that $C_{P_{Ideal}} \propto {C_T}^{\frac{3}{2}}$, as the collective decreases, the ideal power requirement is

expected to fall. Viscous drag is expected to increase in importance compared to the induced drag. The Figure of Merit is therefore expected to drop further once viscous coupling is included into the simulation. It may also be noted that the Figure of Merit begins falling past 11° of collective. This could be caused by viscous and/or compressibility effects (the blade tip Mach number is 0.58). To verify this, the viscous database should be constructed to contain data for various Mach numbers. Viscous drag was added in post-processing to figures 4.11 and 4.12. As expected, this tends to lower the Figure of Merit across all simulations. The drag was calculated based on the lift calculated by the UVLM and the drag polar calculated by X-Foil (Drela, 1989) at $Re = 1e6$. Properly coupling the UVLM to a viscous database is expected to yield better results.

4.2.3 Tip Vortex Position

Figure 4.13 shows the tip vortex position for the parametric sweep of the collective angle. The general tendency of the simulation results is for the tip vortex to contract too far inboard and to descend too slowly. However, certain qualitative aspects can be observed. For example, the axial velocity, represented as the slope of the $\frac{z}{R}$ curve, increases when the collective angle (thrust) increases.

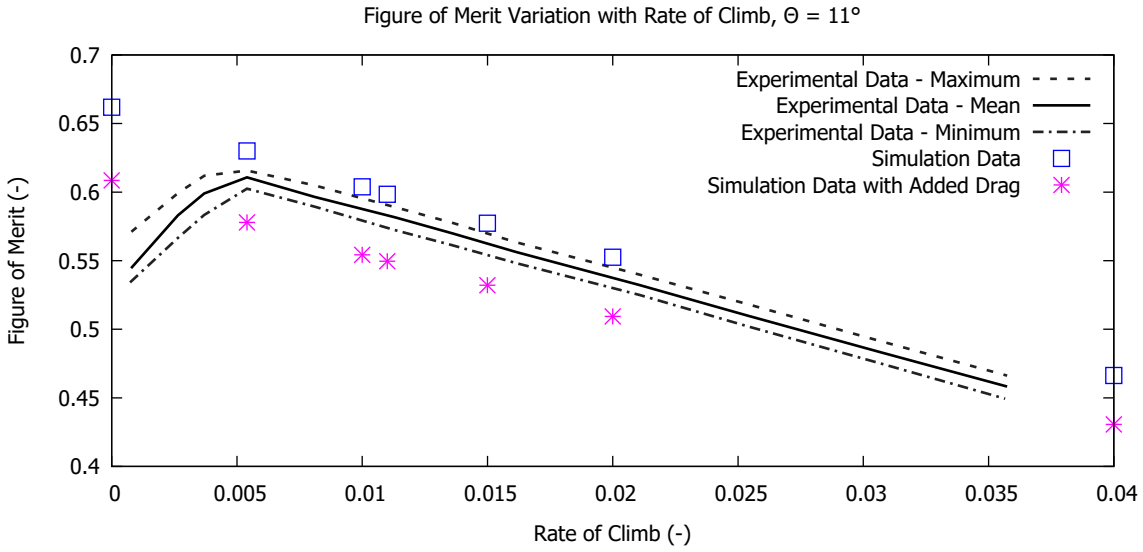

Figure 4.11 Variation of Figure of Merit with Varying Climb Rate and Fixed Collective

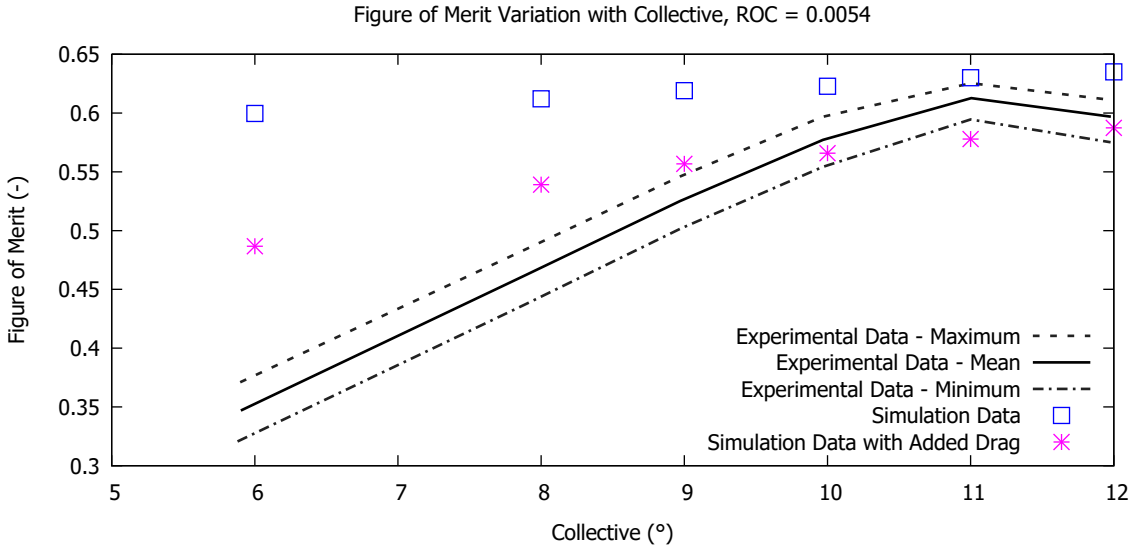

Figure 4.12 Variation of Figure of Merit with Varying Collective and Fixed Climb Rate

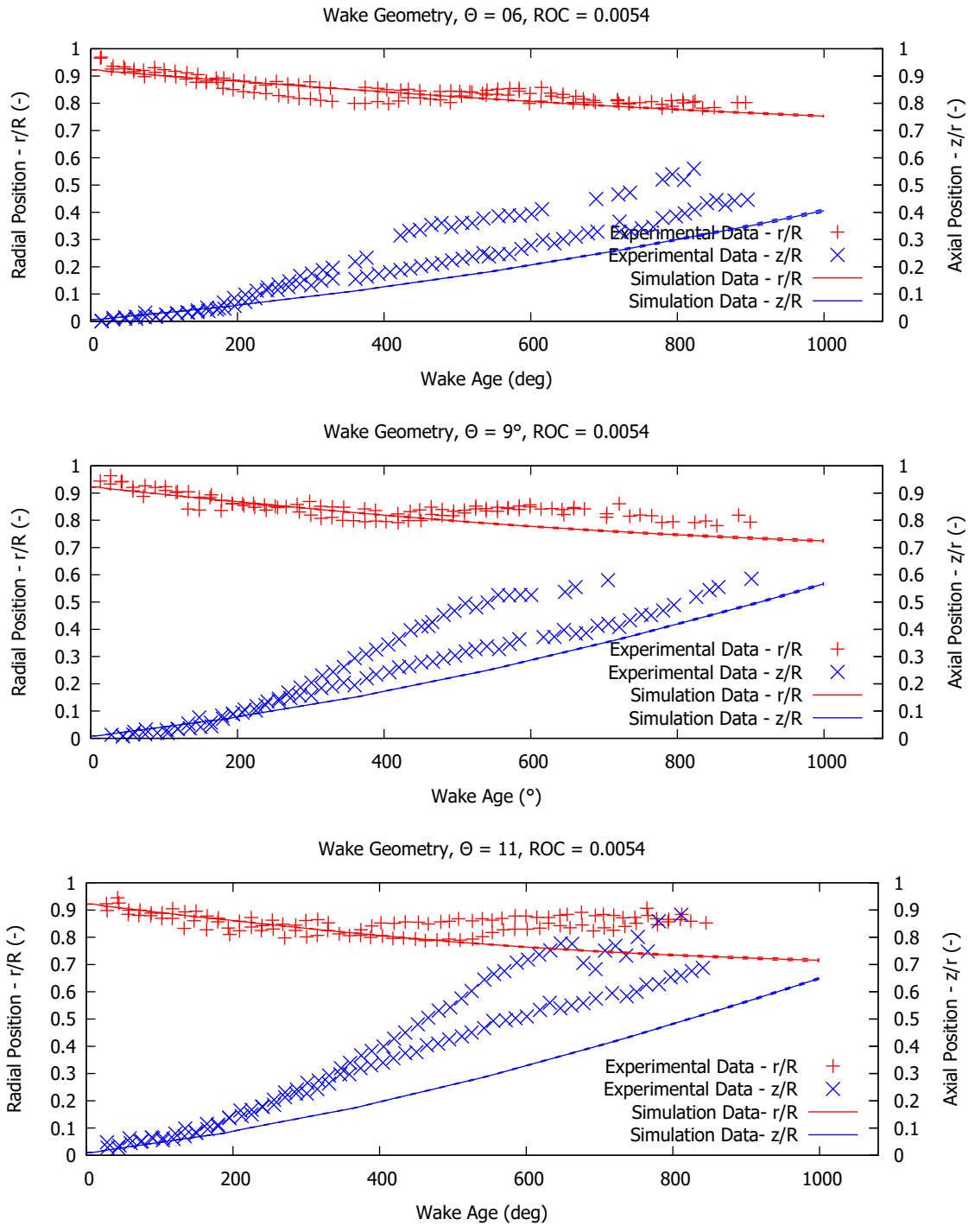

Figure 4.13 Tip Vortex Position for Constant Climb Rate and Varying Collective

4.3 Lynx Tail Rotor in Ground Effect

This test case, as presented by Light (1993), uses a four-bladed rotor usually used as a tail rotor on the Lynx helicopter. The rotor radius is 1.105m, with a cutout at 0.425m. The airfoil has a constant chord of 0.180m and consists of a NPL9615 airfoil. The test places the tail rotor at varying distances from a flat plate, measuring the impact of ground effect on the rotor performance. This test is used to validate the effectiveness of the UVLM at predicting the variation in performance parameters in ground effect. The UVLM was run using a mirror plane to represent the ground. The vortex particle wake was used with a viscous core size $r_c^* = 0.4$. Table 4.9 summarizes the above stated data. The test matrix is presented in table 4.10.

4.3.1 Thrust Comparison

As a helicopter approaches the ground, a large portion of the rotor downwash is pushed outward from beneath the main rotor. This creates a "cushion" of air below the helicopter that increases its hover performance. As presented by Cheeseman and Bennett (1955), the variation of thrust in ground effect may be estimated by

$$\frac{T_{IGE}}{T_{OGE}} = \frac{1}{1 - \frac{1}{16}\left(\frac{R}{h}\right)^2}. \tag{4.3}$$

Figure 4.14 presents a comparison of Cheeseman's equation, the UVLM simulation results and Light's experimental data. The error bars present on the simulation data represent the standard deviation of the thrust ratio over the final two rotations. The simulation results agree reasonably well with experimental data. It should be noted that convergence in ground effect was much more difficult to obtain. In certain cases, as denoted by the long error bars, convergence was not obtained. The convergence issues are due to the proximity of the rotor blades with the wake. While the test conditions place the rotor in extreme ground effect, it

Table 4.9 Lynx Tail Rotor Parameters

Rotor Radius	1.105m
Rotor Root Cutout	0.425m
Blade Chord	0.180m
Airfoil	NPL9615
Rotor Solidity	0.208
Rotation Speed	1660 RPM

Table 4.10 Lynx Tail Rotor Test Matrix

Collective	$\frac{h}{R}$	$\left(\frac{C_T}{\sigma}\right)_{Experimental}$
13°	OGE	0.063
13°	0.84	0.071
13°	0.46	0.077
13°	0.34	0.080
14°	OGE	0.070
14°	1.92	0.070
14°	0.64	0.081
14°	0.42	0.085
14°	0.26	0.090
15°	OGE	0.077
15°	1.54	0.080
15°	0.96	0.084
15°	0.52	0.090
15°	0.32	0.095
16°	OGE	0.085
16°	1.20	0.090
16°	0.72	0.094
16°	0.52	0.099
17°	OGE	0.091
17°	1.92	0.093
17°	0.78	0.102

should be noted that some conditions cannot be replicated with an actual helicopter. This proximity induces large strain on the vortons, leading to numerical divergence in certain cases. It may be required to apply a limiter to the strain equation. Also note that Cheeseman's equation remains valid up to $\frac{h}{R} \approx 0.75$ when compared to the experimental data.

4.3.2 Tip Vortex Position

Figure 4.15 shows the position of the tip vortex in ground effect. It is noted that the tip vortex tends to stagnate near, but not necessarily on, the ground. As previously noted, the axial velocity of the tip vortex seems to be too slow. The radial contraction, however, seems to match the experimental results.

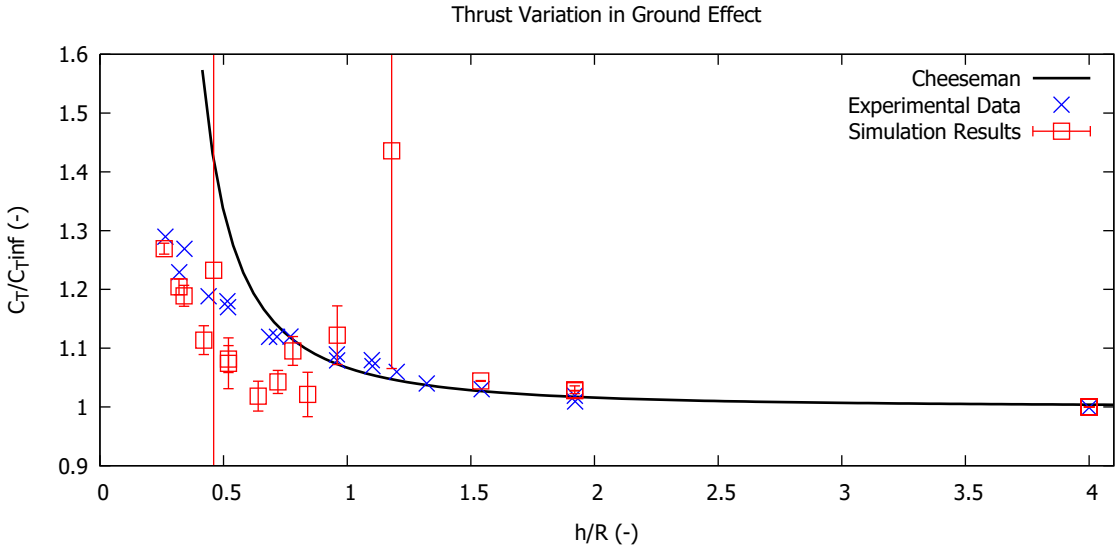

Figure 4.14 Thrust Variation in Ground Effect

4.3.3 Unsteady Phenomena

When simulating a rotor very close to the ground, an unexpected physical phenomenon was captured. The proximity of the rotor to the ground tends to segregate the wake into two portions: the first is sent outboard of the rotor, while the second tends to accumulate beneath the rotor hub. The wake grows beneath the rotor hub until it can no longer be contained. It then releases upward through the rotor hub as a bubble of vorticity. This bubble moves through the air in a toroidal motion. This is indicative of a vortex ring state, captured at the root of the blade. This occurs periodically throughout the simulation, as can be seen in figure 4.16. The formation of vortex rings may only be possible because the rotor hub was not modelled. At the time of writing, Jardin *et al.* (2017) published results for a rotor in ground, ceiling and wall effect. The current code implementation supports these interfaces and would merit further investigation.

Capturing such a complex phenomenon is promising, as it may indicate the ability to simulate descending flight in Vortex Ring State (VRS). The thrust coefficient varies greatly with the release of each vortex ring from the rotor hub. These variations would be expected to be even larger if the vortex rings were to be shed from the rotor tip. Further testing will be required to better understand this phenomenon. Data gathering may be required to provide experimental data for rotors in descending flight.

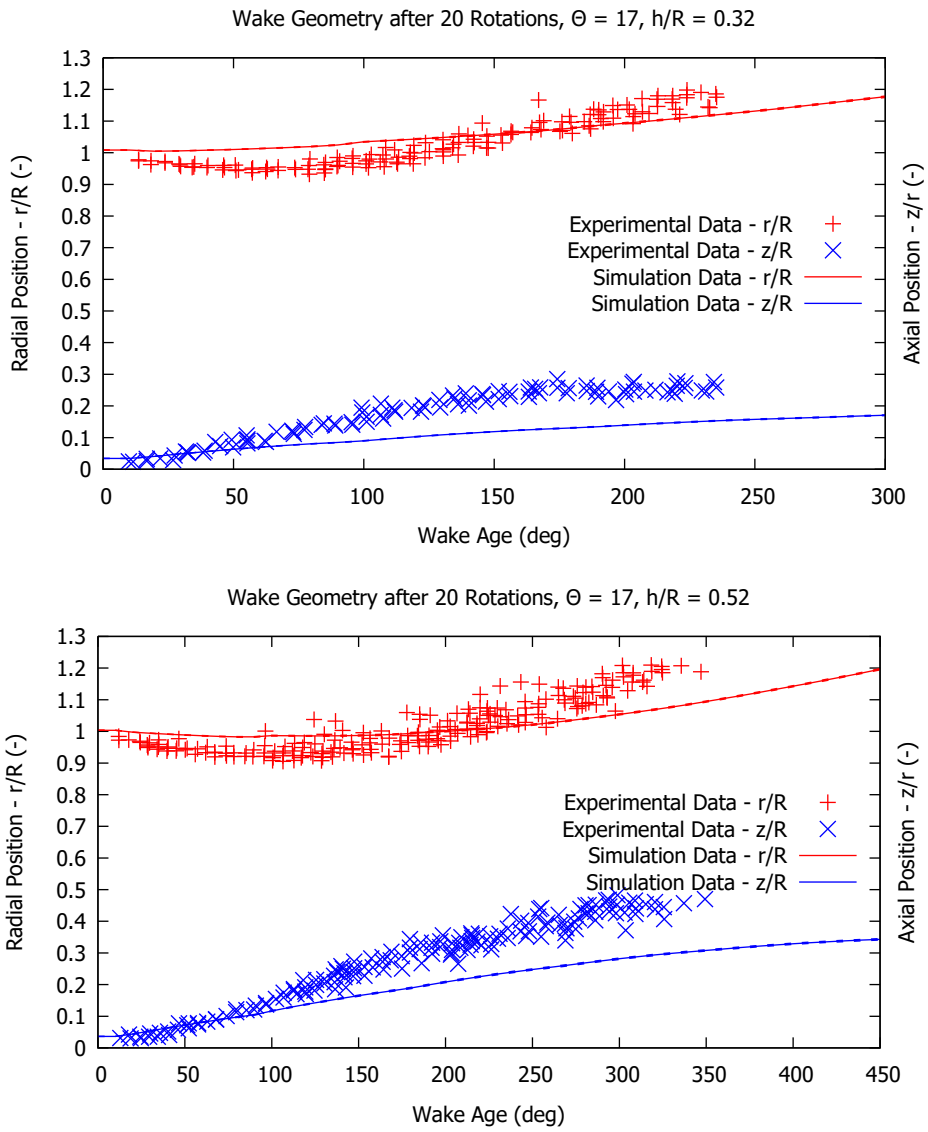

Figure 4.15 Tip Vortex Position in Ground Effect

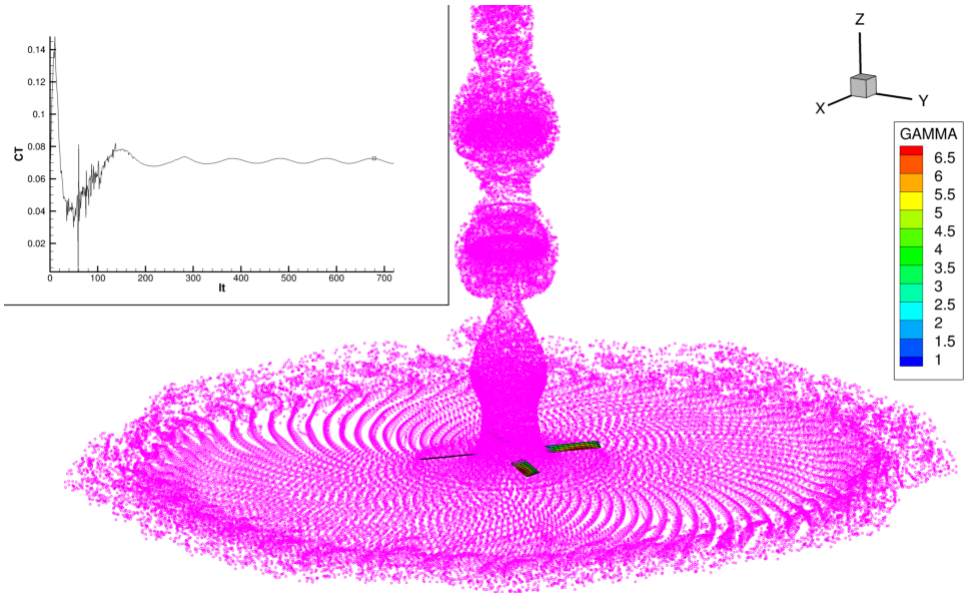

Figure 4.16 Vortex Rings Released from the Rotor Hub

4.4 Summary

In this chapter, the UVLM code was validated against three test cases. The Caradonna-Tung rotor in hover was first used to determine the effect of core size on simulation stability. The Lamb-Oseen and Vorton wake models showed increased stability in thrust convergence and tip vortex position when compared to the Vatistas $n = 2$ and Scully core models. The Vorton wake also stable enough to calculate the required power of the rotor, thus resulting in a stable figure of merit calculation. For this reason, the vorton wake was applied to the Caradonna rotor in climb. The calculated figure of merit showed the same qualitative tendencies as the experimental data. However, certain discrepancies were noted and believed to be caused by the inviscid nature of the UVLM. Coupling the UVLM to a viscous database may improve these results.

The vorton wake was also used in testing ground effect, using Light's experimental data. The increase in thrust noted when the rotor was placed near the ground showed correct tendencies when compared to experimental data. However, numerical stability was an issue in certain conditions. Further investigation is required. Furthermore, the unsteady phenomena of vortex ring generation in ground effect was captured. This is a promising result, as it may allow the study of the dangerous Vortex-Ring State experienced in helicopters in descending flight.

CHAPTER 5 CONCLUSION

This chapter concludes the thesis by providing a synthesis of the discussed work. The limitations of the current methodology are discussed and recommendations for future work are provided.

5.1 Synthesis of Work

The overarching objective of the research project was to develop a numerical model that could determine helicopter performance parameters when landing on a ship. The primary objective of this thesis was to properly model helicopter wakes, as they affect performance calculations. An in-house UVLM code was adapted for rotating lifting surfaces.

The first subobjective consisted of defining a model that could determine the performance of a helicopter in hover and in climb. The study of the effect of various viscous core models on helicopter performance and UVLM numerical stability was the first step to accomplishing this objective. Four different core models were presented. For panel wakes, the Lamb-Oseen core model, the Scully core model and the Vatistas core models were presented. For vortex particle wakes, the algebraic smoothing model was shown. These vortex models were compared when validating the code against the Caradonna-Tung rotor. The Lamb-Oseen core model and the algebraic smoothing core model showed increased convergence speed for the thrust calculation when compared to the Scully and Vatistas core models. Furthermore, the Lamb-Oseen and algebraic smoothing models were relatively insensitive to the initial core size. A study of the tip vortex position for these core models showed similar results, in that the Lamb-Oseen and Algebraic Smoothing core models showed increased convergence in their results than the Scully and Vatistas models.

The effect of various wake models on calculation time and solution accuracy was then studied towards the same objective. When validating the Caradonna-Tung rotor, two wake models were used: the panel wake and the vorton wake. The panel wake with the Lamb-Oseen core model generally matched experimental data, as did the vorton wake model. Between these models, however, the vorton wake was the only method that converged in torque calculation as well. This permitted the calculation of the power coefficient of the rotor and the Figure of Merit. The vorton wake model was therefore used to validate the code against the Caradonna rotor in climb. The calculation of the Figure of Merit show qualitative aspects expected of rotor performance in climb. In particular, a linear decrease of the Figure of Merit is observed

with increasing rate of climb for constant collective pitch. A linear increase in Figure of Merit for increasing collective at a constant rate of climb is also noted.

The second objective was to develop a model that could determine the performance of a helicopter in ground effect. The vortex particle method was used to validate the code with the experimental data provided by Light of a rotor in ground effect. Increased difficulty in obtaining a converged solution was noted. However, the effect of ground proximity on thrust generation is noted. Figure of Merit could not be calculated due to the sensitivity of the drag calculation in the UVLM method. When placing the rotor in extreme proximity to the ground, vortex rings were generated at the rotor hub and were released in periodic cycles, affecting the thrust generated by the rotor. From the obtained results, the vortex particle wake provided the most accurate physical and numerical solutions. However, the vortex particle wake method is also considerably slower than the panel wake method, as it requires the costly evaluation of the velocity gradient at each vorton's position.

5.2 Limitations of the Proposed Solution

While the groundwork has been laid for rotorcraft simulation, the present state of the in-house UVLM code will require additional features before achieving the overall objective of the research proposal: to simulate rotorcraft landing on a ship. There still seems to be a source of numerical instability in the current implementation that will require further investigation to determine the cause. Current application of the simulation is limited to hovering/axial flight due to the lack of cyclic/collective control input. Adding these inputs, along with a trim methodology, would open the door to translational flight. The lack of viscous drag is another limitation of the current model, leading to certain inaccuracies when calculating the power required and the Figure of Merit. Furthermore, closed objects currently need to be modelled with vortex panels, which creates a numerical singularity that needs to be removed by altering the system of equations. The use of source/doublet panels for closed objects would be more appropriate, as this numerical singularity would no longer be present. The code execution time could also be improved, as this limits the amount of wake kept in memory.

5.3 Future Work

In order to improve the simulation capacity of the in-house UVLM code, the following improvements are proposed, issued from the previously stated limitations.

- Investigate the source of instabilities in the current implementation.

- Design and implement cyclic/collective control input and trim method
- Implement viscous coupling
- Redesign code to increase computational efficiency
- Investigate the use of acceleration techniques, such as multipole algorithms (Koumoutsakos, 1995; Nishimura, 2002)

REFERENCES

ANANTHAN, S., LEISHMAN, J. G., and RAMASAMY, M., "The role of filament stretching in the free-vortex modelling of rotor wakes," in *58th Annual Forum and Technology Display of the American Helicopter Society International*. Montreal, Canada, 2002.

ANDERSON, J. D. and WENDT, J., *Computational fluid dynamics*. Springer, 1995, vol. 206.

ANDERSON JR, J. D., *Fundamentals of aerodynamics*. Tata McGraw-Hill Education, 2010.

BAGAI, A. and LEISHMAN, J. G., "Rotor free-wake modeling using a pseudo-implicit technique—including comparisons with experimental data," *Journal of the American Helicopter Society*, vol. 40, no. 3, pp. 29–41, 1995.

BHAGWAT, M. J. and LEISHMAN, J. G., "Generalized viscous vortex model for application to free-vortex wake and aeroacoustic calculations," in *Annual Forum Proceedings-American Helicopter Society*, vol. 58, no. 2. AMERICAN HELICOPTER SOCIETY, INC, 2002, pp. 2042–2057.

BLAZEK, J., *Computational Fluid Dynamics: Principles and Applications:(Book with accompanying CD)*. Elsevier, 2005.

CARADONNA, F., "Performance measurement and wake characteristics of a model rotor in axial flight," *Journal of the American Helicopter Society*, vol. 44, no. 2, pp. 101–108, 1999.

CARADONNA, F. and TUNG, C., "Experimental and analytical studies of a model helicopter rotor in hover," 1981, technical memorandum NASA-TM-81232, California:NASA.

CEBECI, T., SHAO, J. P., KAFYEKE, F., and LAURENDEAU, E., *Computational fluid dynamics for engineers*. Springer Berlin Heidelberg, 2005.

CHEESEMAN, I. and BENNETT, W., "The effect of ground on a helicopter rotor in forward flight," 1955.

CHRUST, M., LAURENDEAU, E., and OSTIGUY, L., "Accelerating low-fidelity aerodynamic codes on multi-and many-core architectures," *The Journal of Supercomputing*, vol. 71, no. 9, pp. 3456–3481, 2015.

CONLISK, A., "Modern helicopter rotor aerodynamics," *Progress in aerospace sciences*, vol. 37, no. 5, pp. 419–476, 2001.

COSTES, M. and KOWANI, G., "An automatic anti-diffusion method for vortical flows based on vorticity confinement," *Aerospace Science and Technology*, vol. 7, no. 1, pp. 11–21, 2003.

CUMMINGS, R. M., BERTIN, J. J., and SMITH, M. L., *Aerodynamics for engineers*. Prentice-Hall, 1998.

DRELA, M., "Xfoil: An analysis and design system for low reynolds number airfoils," in *Low Reynolds number aerodynamics*. Springer, 1989, pp. 1–12.

DUMITRESCU, H. and FRUNZULICA, F., "Free-wake aerodynamic model for helicopter rotors," *Proceedings of the Romanian Academy*, vol. 5, no. 3, pp. 1–9, 2004.

EGOLF, T. A., RAJMOHAN, N., REED, E., and SANKAR, L., "A hybrid cfd method for coaxial rotor performance prediction in forward flight," in *AHS Specialist's Conference on Aeromechanics*, 2010.

GALLAY, S. and LAURENDEAU, E., "Nonlinear generalized lifting-line coupling algorithms for pre/poststall flows," *AIAA Journal*, vol. 53, no. 7, pp. 1784–1792, 2015.

HARIHARAN, N. S., EGOLF, T. A., NARDUCCI, R., and SANKAR, L. N., "Helicopter rotor aerodynamic modeling in hover: Aiaa standardized hover evaluations," in *53rd AIAA Aerospace Sciences Meeting*, 2015, p. 1242.

HORN, J. F., BRIDGES, D. O., WACHSPRESS, D. A., and RANI, S. L., "Implementation of a free-vortex wake model in real-time simulation of rotorcraft," *Journal of Aerospace Computing, Information, and Communication*, vol. 3, no. 3, pp. 93–107, 2006.

JARDIN, T., PROTHIN, S., and MAGAÑA, C. G., "Aerodynamic performance of a hovering microrotor in confined environment," *Journal of the American Helicopter Society*, vol. 62, no. 2, pp. 1–7, 2017.

JOHNSON, W., *Helicopter theory*. Courier Corporation, 2012.

KATZ, J. and PLOTKIN, A., *Low-speed aerodynamics*. Cambridge university press, 2001, vol. 13.

KOUMOUTSAKOS, P., "Fast multipole methods for three-dimensional n-body problems," 1995.

LAMBERTENGHI, A., EMMANUELE, C., FRISCO, N., SCALA, S., PARNISARI, G., BORGATELLI, F., and MOLINARI, D., "Wind characterization around offshore platform for real-time helicopter simulator," 2015, the 3rd OpenFOAM User Conference 2015. [Online]. Available: https://www.slideshare.net/StefanoScala/wind-characterization-around-offshore-platform-for-realtime-helicopter-simulator

LANDGREBE, A. J., "The wake geometry of a hovering helicopter rotor and its influence on rotor performance," *Journal of the American Helicopter Society*, vol. 17, no. 4, pp. 3–15, 1972.

LEISHMAN, J. G., BHAGWAT, M. J., and BAGAI, A., "Free-vortex filament methods for the analysis of helicopter rotor wakes," *Journal of aircraft*, vol. 39, no. 5, pp. 759–775, 2002.

LIGHT, J. S., "Tip vortex geometry of a hovering helicopter rotor in ground effect," *Journal of the American helicopter society*, vol. 38, no. 2, pp. 34–42, 1993.

LINDSAY, K. and KRASNY, R., "A particle method and adaptive treecode for vortex sheet motion in three-dimensional flow," *Journal of Computational Physics*, vol. 172, no. 2, pp. 879–907, 2001.

NISHIMURA, N., "Fast multipole accelerated boundary integral equation methods," *Applied Mechanics Reviews*, vol. 55, no. 4, pp. 299–324, 2002.

PARENTEAU, M., "Aerodynamic optimization of aircraft wings using a coupled vlm-2.5 d rans approach," Ph.D. dissertation, École Polytechnique de Montréal, 2017.

PARENTEAU, M., SERMEUS, K., and LAURENDEAU, E., "Vlm coupled with 2.5 d rans sectional data for high-lift design," in *2018 AIAA Aerospace Sciences Meeting*, 2018, p. 1049.

QUACKENBUSH, T. R., BLISS, D. B., WACHSPRESS, D. A., BOSCHITSCH, A. H., and CHUA, K., "Computation of rotor aerodynamic loads in forward flight using a full-span free wake analysis," 1990.

QUARTERONI, A., SACCO, R., and SALERI, F., *Numerical mathematics*. Springer Science & Business Media, 2010, vol. 37.

RAJMOHAN, N., *Application of hybrid methodology to rotors in steady and maneuvering flight*. Georgia Institute of Technology, 2010.

SQUIRE, H., "The growth of a vortex in turbulent flow," *The Aeronautical Quarterly*, vol. 16, no. 3, pp. 302–306, 1965.

SRIVASTAVA, A. and MOOK, D. T., "Redundancy in the discrete-vortex method for closed bodies," *Journal of Aircraft*, vol. 31, no. 6, pp. 1436–1437, 1994. [Online]. Available: https://doi.org/10.2514/3.46676

STEINHOFF, J. and UNDERHILL, D., "Modification of the euler equations for "vorticity confinement": Application to the computation of interacting vortex rings," *Physics of Fluids*, vol. 6, no. 8, pp. 2738–2744, 1994.

STEPNIEWSKI, W. Z. and KEYS, C., *Rotary-wing aerodynamics*. Courier Corporation, 1979.

TAN, J.-f. and WANG, H.-w., "Simulating unsteady aerodynamics of helicopter rotor with panel/viscous vortex particle method," *Aerospace Science and Technology*, vol. 30, no. 1, pp. 255–268, 2013.

THEOPHANIDES, M. and SPIRA, D., "An object-oriented framework for blade element rotor modelling and scaleable flight mechanics simulation," in *35th European Rotorcraft Forum*. Hamburg, Germany, 2009.

VERSTEEG, H. K. and MALALASEKERA, W., *An introduction to computational fluid dynamics: the finite volume method*. Pearson Education, 2007.

WIE, S. Y., LEE, S., and LEE, D. J., "Potential panel and time-marching free-wake-coupling analysis for helicopter rotor," *Journal of Aircraft*, vol. 46, no. 3, pp. 1030–1041, 2009.

WILLIS, D. J., PERAIRE, J., and WHITE, J. K., "A combined pfft-multipole tree code, unsteady panel method with vortex particle wakes," *International Journal for numerical methods in fluids*, vol. 53, no. 8, pp. 1399–1422, 2007.

WINCKELMANS, G. and LEONARD, A., "Contributions to vortex particle methods for the computation of three-dimensional incompressible unsteady flows," *Journal of Computational Physics*, vol. 109, no. 2, pp. 247–273, 1993.

YOUNG, C., *The prediction of helicopter rotor hover performance using a prescribed wake analysis*. HM Stationery Office, 1974.